The Astrophysical Journal, 838:19 (19pp), 2017 March 20 https://doi.org/10.3847/1538-4357/aa6258

Predicting Quiescence: The Dependence of Specific Star Formation Rate on Galaxy Size and Central Density at $0.5 < z < 2.5$

Katherine E. Whitaker[1,2,10], Rachel Bezanson[3,10,11], Pieter G. van Dokkum[4], Marijn Franx[5], Arjen van der Wel[6], Gabriel Brammer[7], Natascha M. Förster-Schreiber[8], Mauro Giavalisco[1], Ivo Labbé[4], Ivelina G. Momcheva[7], Erica J. Nelson[8], and Rosalind Skelton[9]
[1] Department of Astronomy, University of Massachusetts, Amherst, MA 01003, USA; kwhitaker@astro.umass.edu
[2] Department of Physics, University of Connecticut, Storrs, CT 06269, USA
[3] Steward Observatory, Department of Astronomy, University of Arizona, AZ 85721, USA
[4] Department of Astronomy, Yale University, New Haven, CT 06520, USA
[5] Leiden Observatory, Leiden University, P.O. Box 9513, 2300 RA Leiden, The Netherlands
[6] Max-Planck Institut für Astronomie, Königstuhl 17, D-69117, Heidelberg, 0000-0002-5027-0135, Germany
[7] Space Telescope Science Institute, Baltimore, MD 21218, USA
[8] Max-Planck-Institut für extraterrestrische Physik, Giessenbachstrasse, D-85748 Garching, Germany
[9] South African Astronomical Observatory, P.O. Box 9, Observatory, Cape Town, 7935, South Africa
[10] Department of Astrophysics, Princeton University, Princeton, NJ 08544, USA
Received 2016 July 11; revised 2017 January 28; accepted 2017 February 20; published 2017 March 20

Abstract

In this paper, we investigate the relationship between star formation and structure, using a mass-complete sample of 27,893 galaxies at $0.5 < z < 2.5$ selected from 3D-*HST*. We confirm that star-forming galaxies are larger than quiescent galaxies at fixed stellar mass ($M_\star$). However, in contrast with some simulations, there is only a weak relation between star formation rate (SFR) and size within the star-forming population: when dividing into quartiles based on residual offsets in SFR, we find that the sizes of star-forming galaxies in the lowest quartile are 0.27 ± 0.06 dex smaller than the highest quartile. We show that 50% of star formation in galaxies at fixed $M_\star$ takes place within a narrow range of sizes (0.26 dex). Taken together, these results suggest that there is an abrupt cessation of star formation after galaxies attain particular structural properties. Confirming earlier results, we find that central stellar density within a 1 kpc fixed physical radius is the key parameter connecting galaxy morphology and star formation histories: galaxies with high central densities are red and have increasingly lower $\mathrm{SFR}/M_\star$, whereas galaxies with low central densities are blue and have a roughly constant (higher) $\mathrm{SFR}/M_\star$ at a given redshift. We find remarkably little scatter in the average trends and a strong evolution of >0.5 dex in the central density threshold correlated with quiescence from $z \sim 0.7$–2.0. Neither a compact size nor high-n are sufficient to assess the likelihood of quiescence for the average galaxy; instead, the combination of these two parameters together with $M_\star$ results in a unique quenching threshold in central density/velocity.

Key words: galaxies: evolution – galaxies: formation – galaxies: high-redshift – galaxies: structure

1. Introduction

Despite decades of deep and wide extragalactic surveys, we still do not understand the astrophysics behind the empirical relationship linking the star formation histories of galaxies and their morphologies. Observations show that galaxies with evolved stellar populations, so-called "quiescent" galaxies, have significantly smaller sizes and more concentrated light profiles than actively star-forming galaxies with a similar stellar mass and redshift (e.g., Shen et al. 2003; Trujillo et al. 2007; Cimatti et al. 2008; Kriek et al. 2009; Williams et al. 2010; Wuyts et al. 2011b; van der Wel et al. 2014). Although we know that galaxies must shut down their star formation and migrate from the star-forming to quiescent population, there is much to be learned about the physical process(es) that are primarily responsible for this structural evolution and the quenching of star formation.

One way to study the connection between this bimodal population of galaxies is through correlations between specific star formation rate ($\mathrm{sSFR} \equiv \mathrm{SFR}/M_\star$) and parameters describing various physical properties of galaxies, such as stellar mass (e.g., Whitaker et al. 2014; Schreiber et al. 2015), surface density (e.g., Franx et al. 2008; Barro et al. 2013), bulge mass (e.g., Bluck et al. 2014; Lang et al. 2014; Schreiber et al. 2016), or environment (e.g., Elbaz et al. 2007). The inverse of the sSFR defines a timescale for the formation of the stellar population of a galaxy, where lower sSFRs correspond to older stellar populations for a constant or single-burst star formation history. In this sense, sSFR is a relatively straightforward diagnostic of quiescence that can be directly linked to other physical properties of galaxies.

With a sample of galaxies selected from the Sloan Digital Sky Survey (SDSS), Brinchmann et al. (2004) were the first to show that there is a turnover in the sSFR of galaxies at higher stellar surface mass densities (also studied in the context of a turnover in $D_n(4000)$ by Kauffmann et al. 2003b). The redshift evolution of this correlation was later presented in Franx et al. (2008) (see also Maier et al. 2009). Both works identified a threshold surface density at each redshift interval: below this threshold the sSFRs are high with little variation, and above the threshold density, galaxies have low sSFRs. Franx et al. (2008) reported that the density threshold increases with redshift, at least out to $z = 3$. As stellar density and velocity dispersion are closely related (e.g., Wake et al. 2012; Fang et al. 2013), observations therefore indicate that galaxies are statistically more likely to be quiescent once they have surpassed a threshold in either density or velocity dispersion. Studies of early-type galaxies at $z \sim 0$ further show that at fixed stellar mass, the velocity dispersion is strongly correlated with other

[11] Hubble Fellow.

physical properties: galaxies with increased velocity dispersion and thereby more compact sizes are on average older, more metal-rich, have lower molecular gas fractions, and are more alpha-enhanced than their larger counterparts with lower velocity dispersions (Thomas et al. 2005; Cappellari et al. 2013; McDermid et al. 2015).

Bezanson et al. (2009) showed that the densities of distant compact galaxies are similar to those of the central regions of these local early-type galaxies. The authors compared the average stellar density profiles of distant compact galaxies within a constant physical radius of 1 kpc (see also van Dokkum et al. 2010, 2014; Saracco et al. 2012; Tacchella et al. 2015a). This study was the first to present a plausible link between these high-redshift galaxies and their final location in the local universe, but the cause of the quenching is still unclear. This work suggests, however, that it may be more reliable to define a quenching threshold in surface density within the central 1 kpc, as opposed to the half-light radius. Fang et al. (2013) found that this central density threshold increases with stellar mass through a study of the correlation between galaxy structure and the quenching of star formation using a sample of SDSS central galaxies. Furthermore, studies that push the analysis of the central density out to $z = 3$ corroborate this result (e.g., Cheung et al. 2012; Saracco et al. 2012; Barro et al. 2013, 2015), supporting the idea that the innermost structure of galaxies is most likely physically linked with quenching. Where the earlier work of Franx et al. (2008) found an evolving effective surface density threshold with redshift, Barro et al. (2015) did not find a strong redshift evolution in the central surface density threshold. However, as star-forming galaxies still exist above this quenching threshold, results in the literature conclude that a dense bulge is a necessary but insufficient condition to fully quench galaxies (see also Bell et al. 2012).

While most studies have focused on the the stellar mass dependence of the central density alone, it is perhaps unsurprising that there is a tight correlation: the central density is a biproduct of the combined stellar mass and light profile. The key comparison instead should be made with the sSFR, normalizing out the stellar mass dependence of SFR (as also studied in Barro et al. 2015), where total sSFRs can be measured largely independently of the central density. While the dynamic range in stellar mass enabled by the deep high-resolution near-infrared (NIR) imaging from the Cosmic Assembly Near-IR Deep Extragalactic Legacy Survey (CANDELS; Grogin et al. 2011; Koekemoer et al. 2011) dramatically improves the results compared to earlier multiwavelength extragalactic surveys (e.g., Wuyts et al. 2008; Whitaker et al. 2012b), the depth of the *Spitzer*/MIPS 24 μm imaging used to derive the IR SFR indicator has remained unchanged. To therefore use the full range in stellar mass and galaxy structure probed by these *Hubble Space Telescope* legacy programs, we must perform a detailed stacking analyses of the 24 μm imaging to probe the SFR properties of the complete unbiased sample of galaxies using a single reliable star formation rate (SFR) indicator (e.g., Whitaker et al. 2015).

By combining the high-resolution photometry from CANDELS with the accurate spectroscopic information provided by the 3D-*HST* treasury program (Brammer et al. 2012; Momcheva et al. 2016) and a stacking analysis of the unobscured (UV) and obscured (IR) SFRs, we are in a unique position to perform a census across most of cosmic time of the simultaneous evolution of galaxy structure and star formation. While earlier results from this treasury data set have shown that all quiescent galaxies have a dense stellar core and that the formation of such cores is a requirement for quenching (van Dokkum et al. 2014; Barro et al. 2015; Whitaker et al. 2015), there are several open questions that we aim to answer in this paper. Specifically, (1) how does SFR depend on galaxy size? (2) Is there a preferential galaxy size scale where star formation occurs? (3) Is there a physical parameter that will uniquely predict quiescence? And (4), does the quenching threshold in surface density and velocity evolve with redshift? There are a few differences that together separate the present analysis from earlier studies: the inclusion of accurate grism redshifts from 3D-*HST* improve the stellar population parameters, we derive the three-dimensional deprojected central density and circular velocity instead of the surface density, and we stack the 24 μm imaging to reliably measure total SFRs for more extended galaxies with lower stellar mass or low SFR.

The paper is outlined as follows. In Section 2 we introduce the data and sample selection, describing the details of the stellar masses, redshifts, rest-frame colors, structural parameters, total SFRs, central densities, and circular velocities. We present the correlations between galaxy size, stellar mass, and sSFR for the overall population in Section 3.1. In Section 3.2 we determine the galaxy size scale at which the majority of star formation occurs from $z = 0.5$ to $z = 2.5$. In Section 3.3 we proceed to analyze the residual offsets in SFR and size for star-forming galaxies alone when the well-known correlations between log(SFR)–log($M_\star$) and log(r_e)–log($M_\star$) are removed. In the second half of the paper, we explore the physical parameters that best predict quiescence. First, we consider the role of galaxy size and Sérsic index in predicting quiescence in Section 4.1. Next, we study in Section 4.2 the dependence of sSFR on stellar mass density, parameterizing the redshift evolution in Section 4.3, and the density and velocity quenching thresholds in Section 4.4. As this paper touches on a relatively wide range of topics, we integrate the discussion and implications of the results throughout the relevant sections, as well as further discussion in Section 5. While we choose to place these empirical results in the context of current theoretical models, we note that many of the correlations that we discuss can be interpreted in a different way (e.g., Abramson & Morishita 2016; Lilly & Carollo 2016). We caution that it is unclear as yet whether there truly is an evolutionary sequence that causally links galaxy structure with star formation. We conclude the paper with a summary in Section 6 of the results we present, in the context of current and future studies of galaxy formation and evolution.

We use a Chabrier (2003) initial mass function and assume a ΛCDM cosmology with $\Omega_M = 0.3$, $\Omega_\Lambda = 0.7$, and $H_0 = 70\ \mathrm{km\ s^{-1}\ Mpc^{-1}}$. All magnitudes are given in the AB system.

2. Data and Sample Selection

2.1. Stellar Masses, Redshifts, and Rest-frame Colors

We use the exquisite *HST* Wide Field Camera 3 (WFC3) multiwavelength photometric and spectroscopic data sets of five well-studied extragalactic fields through the CANDELS and 3D-*HST* surveys. Using stellar masses, redshifts, and rest-frame colors from the 3D-*HST* 0.3–8 μm photometric catalogs (see Skelton et al. 2014, for full details), we select samples in three redshift intervals of $0.5 < z < 1.0$, $1.0 < z < 1.5$, and

$1.5 < z < 2.5$: 11266, 9553, and 7791 galaxies above the stellar mass limits for star-forming galaxies. When splitting the sample into subpopulations and accounting for stellar mass limits, our sample is further reduced to 9694 (1192), 8643 (705), and 6893 (766) star-forming (quiescent) galaxies greater than stellar mass limits of $\log M_\star/M_\odot = 8.6(9.0)$, 8.8 (9.4), and 9.4 (10.0), respectively. The galaxies are defined to be either star-forming or quiescent based on their rest-frame $U - V$ and $V - J$ colors, following the definition of Whitaker et al. (2012a). We have identified and removed luminous active galactic nuclei (AGNs) using the *Spitzer*/IRAC color selections presented in Donley et al. (2012), as they may have significant contamination of their IR SFR; only 2% of the sample were removed as AGN candidates. The total sample comprises 27,893 galaxies at $0.5 < z < 2.5$.

We only analyze data that are mass-complete for star-forming galaxies. The lower bounds of the stellar mass limits correspond to the mass-completeness limits down to which van der Wel et al. (2014) were able to determine structural parameters for star-forming and quiescent galaxies with good fidelity. The values for star-forming galaxies are in agreement with the mass-completeness limits presented in Tal et al. (2014), which are determined by comparing object detection in CANDELS/deep with a recombined subset of the exposures that reach the depth of CANDELS/wide. We indicate the stellar mass limits from van der Wel et al. (2014) to which we can trust the star-forming and quiescent structural measurements in Figures 1 and 2. We additionally correct the stellar masses of star-forming galaxies for contamination of the broadband fluxes from emission lines using the values presented in Appendix A of Whitaker et al. (2014). These corrections only begin to become significant at $\log M_\star/M_\odot < 9.5$ and $z > 1.5$.

Where available, we combine the spectral energy distributions (SEDs) with low-resolution *HST*/WFC3 G141 grism spectroscopy to derive grism redshifts with 0.3% accuracy (Brammer et al. 2012). Momcheva et al. (2016) presented the full details of the 3D-*HST* grism data reduction and redshift analysis. We select the "best" redshift to be the spectroscopic redshift, grism redshift, or photometric redshift in this ranked order depending on the availability. Photometric redshifts comprise 52% (57%) of the $0.5 < z < 1.5$ ($1.5 < z < 2.5$) sample, while 39% (40%) have grism redshifts, and 9% (2%) have spectroscopic redshifts.

2.2. Structural Parameters

Size and Sérsic indices used herein are measured from deep *HST*/WFC3 $J_{\rm F125W}$ and $H_{\rm F160W}$ photometry, as presented in van der Wel et al. (2012, 2014). The structural measurements are parameterized profile fits that implicitly take into account the *HST*/WFC3 point-spread function at the time of the measurement. These measurements therefore do not require systematic corrections of more than a few percent (see Section 2.5 in van der Wel et al. 2012), and represent the size (and Sérsic index) distribution with good fidelity across the examined redshift range. The effective radius in each filter is defined to be the semimajor axis of the ellipse that contains half of the total flux of the best-fitting Sérsic model. van der Wel et al. (2014) parameterized the effective radius as a simple function of redshift and stellar mass (their Equations (1) and (2)). Following Equation (1) in van der Wel et al. (2014), the rest-frame 5000 Å effective radius for galaxies with $z < 1.5$ is measured from the $J_{\rm F125W}$ effective radius, whereas $H_{\rm F160W}$ is used at $z > 1.5$. Similarly, we adopt the Sérsic indices measured from the $J_{\rm F125W}$ photometry at $0.5 < z < 1.5$ and $H_{\rm F160W}$ at $1.5 < z < 2.5$ (see Whitaker et al. 2015, for details) for the central density measurement in Section 2.4. The details of the error analysis on r_e and n are presented in van der Wel et al. (2012).

2.3. Total Star Formation Rates

Total SFRs are derived from median stacks of *Spitzer*/MIPS 24 μm photometry, following the procedure detailed in Whitaker et al. (2014). The *Spitzer*/MIPS 24 μm images in the AEGIS field are provided by the Far-Infrared Deep Extragalactic Legacy (FIDEL) survey (Dickinson & FIDEL Team 2007), COSMOS from the S-COSMOS survey (Sanders et al. 2007), GOODS-N and GOODS-S from Dickinson et al. (2003), and UDS from the *Spitzer* UKIDSS Ultra Deep Survey[12] (SpUDS; PI: J. Dunlop).

Briefly, the analysis code uses a high-resolution $J_{\rm F125W}+H_{\rm F140W}+H_{\rm F160W}$ detection image as a prior to model the contributions from neighboring blended sources in the lower resolution MIPS 24 μm image. All galaxies are "cleaned" of the contaminating flux of the neighboring sources before stacking. We refer the reader to Section 3 of Whitaker et al. (2014) for the full details of the MIPS 24 μm stacking analyses. The SFRs derived for quiescent galaxies herein are most likely upper limits because the 24 μm technique tends to overestimate the SFRs for galaxies with $\log {\rm sSFR} < -10\,{\rm yr}^{-1}$ (Fumagalli et al. 2014; Hayward et al. 2014; Utomo et al. 2014). We note that the UV+IR SFR technique is generally reliable for star-forming galaxies. We derive uncertainties in the average SFRs from 50 Monte Carlo bootstrap simulations of the stacking analyses. The error in the mean is therefore the width of the resulting distribution of SFRs divided by the square root of the number of galaxies in each bin.

We choose to use the *Spitzer*/MIPS 24 μm IR SFR because of the resolution and depth of the observations, and to mitigate systematic uncertainties when combining different SFR indicators. However, we note that the observed 24 μm samples major spectral features arising from polycyclic aromatic hydrocarbons (PAHs). Despite complications from these PAH features, Wuyts et al. (2011a) demonstrated that the luminosity-independent conversion from 24 μm to the bolometric IR luminosity used here yields estimates that are in good median agreement with measurements from *Herschel*/PACS photometry (see also Tomczak et al. 2016, and B. Lee et al. 2017, in preparation). When combining the 24 μm IR SFR indicator with the rest-frame UV, we can therefore successfully recover the average total amount of star formation in galaxies. While considering the average correlations and including a bootstrap error analysis will reduce the potential noise in these measurements, we cannot rule out that there exist biases that are due to the physical conditions of the dust and the star formation itself that are incredibly difficult to quantify.

2.4. Central Density

Given the observed projected two-dimensional surface density, the surface brightness distribution can be deprojected to obtain a three-dimensional light distribution if we assume spherical symmetry. We derived this three-dimensional density

[12] http://irsa.ipac.caltech.edu/data/SPITZER/SpUDS/

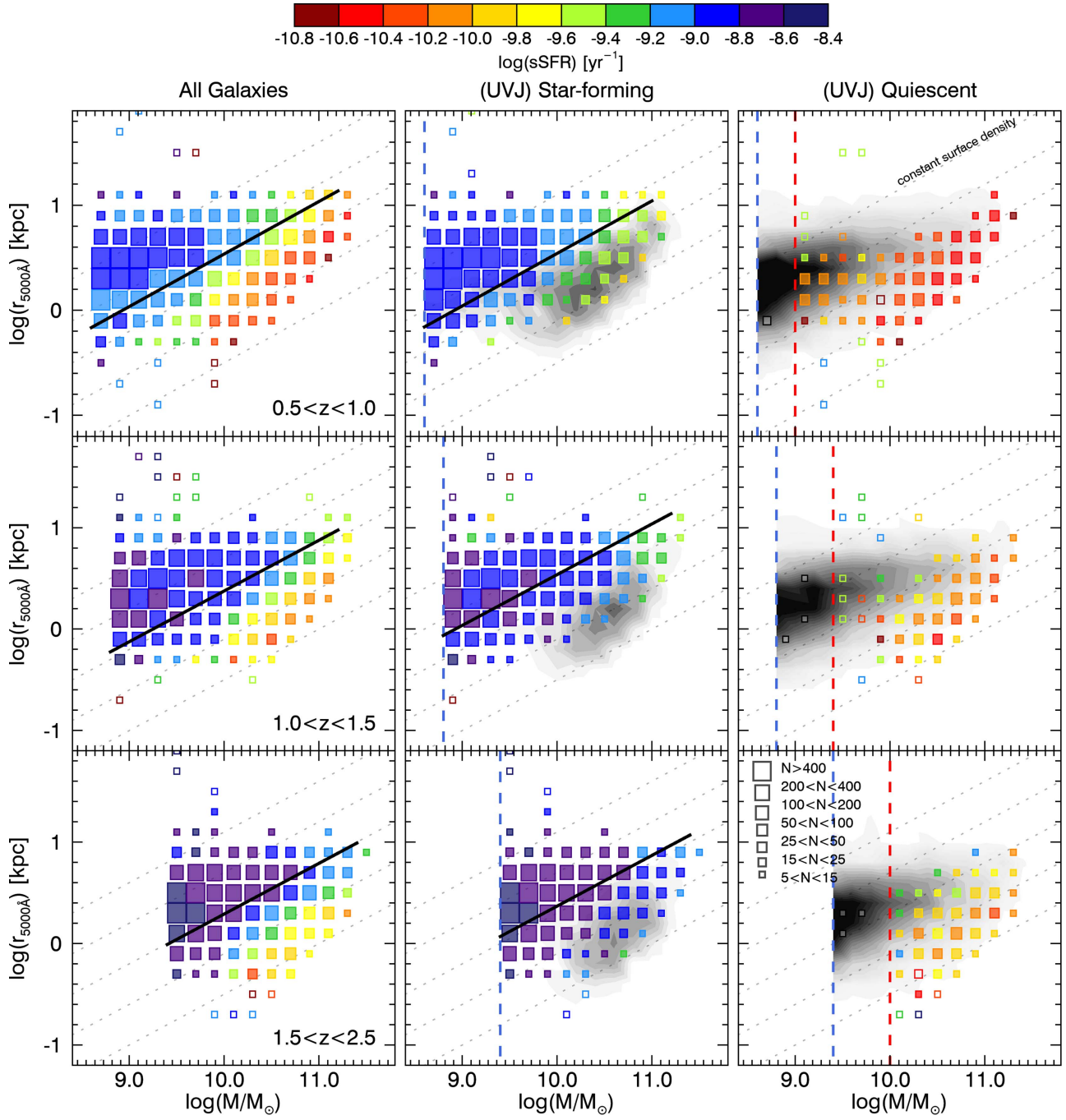

Figure 1. Rest-frame 5000 Å size of galaxies as a function of stellar mass, color-coded by the sSFRs derived from UV+IR median stacking analyses in 0.2 dex bins of $\log M_\star/M_\odot$ and $\log r_{5000\,\text{Å}}$. The size of the symbol depends on the number of galaxies that enter each bin. The vertical dashed lines correspond to the stellar mass limits down to which the structural parameters can be trusted for star-forming (blue) and quiescent (red) populations. The black dotted lines correspond to lines of constant surface density, stellar mass per unit area, with the solid line corresponding to the characteristic central density measured in Figure 9.

profile from the best-fit structural parameters to the intensity profiles of the individual galaxies described in Section 2.2. The projected luminosity within a projected radius is described in Ciotti (1991), assuming isotropic spherical galaxies with surface luminosity profiles following the Sérsic profile. We adopted the asymptotic approximation for the term b_n from Ciotti & Bertin (1999). This asymptotic expansion is truncated to the first four terms and is accurate to 6×10^{-7} for exponential disks ($n = 1$) and 10^{-7} for a de Vaucouleur profile ($n = 4$). The approximation for b_n presented in Ciotti & Bertin (1999) performs much better than previous formulae (e.g., Ciotti 1991, and others). However, despite the accuracy of the asymptotic expansion, we note that this method may lead to errors for galaxies that are far from the assumed spherical symmetry, in particular for flat disks. We return to this issue in Section 4.2.

Following the equations summarized in Section 2.2 of Bezanson et al. (2009), we performed an Abel Transform to deproject the circularized three-dimensional light profile. Assuming mass follows the light and there are no strong color

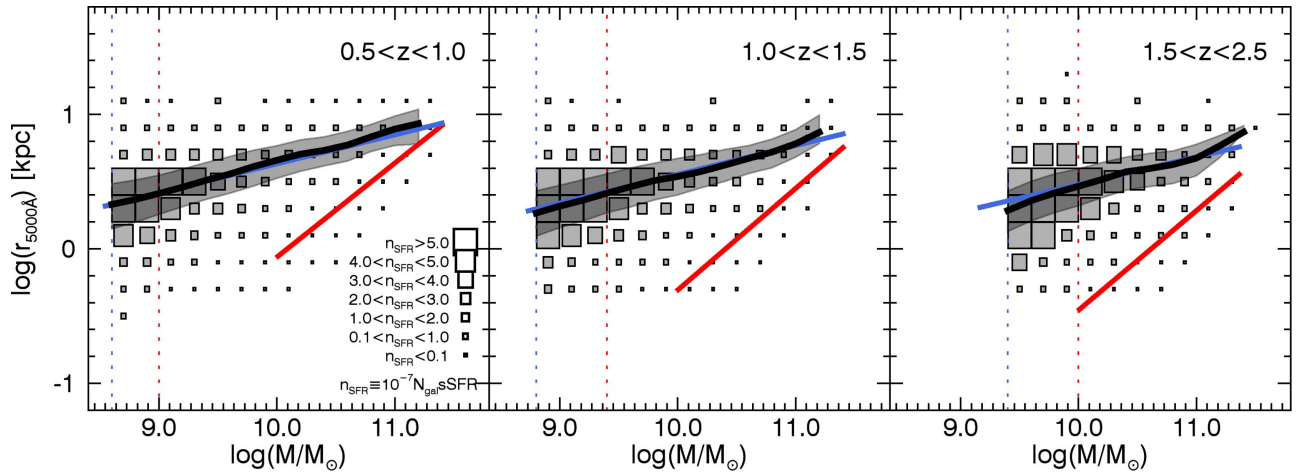

Figure 2. The galaxy size–mass plane at $0.5 < z < 1.0$, $1.0 < z < 1.5$, and $1.5 < z < 2.5$, with symbol sizes representing the total contribution to the star formation budget. The size of each symbol is set by the number of galaxies within each 0.2 dex bin of $\log M_\star/M_\odot$ and $\log r_{5000\,\text{Å}}$, multiplied by the median UV+IR specific SFR. The black line demarcates the 50th percentile, signifying the size scale at which half of the star formation for a given stellar mass galaxy is occurring. The gray shaded region shows the 25th and 75th percentiles, showing that most of the star formation in the universe occurs within a relatively narrow range in galaxy sizes. The blue and red lines are the average size–mass relations for star-forming and quiescent galaxies from van der Wel et al. (2014), respectively.

gradients, the total luminosity is converted into a total stellar mass using the stellar masses presented in Skelton et al. (2014). These stellar masses (labeled M_{phot} below) are derived by modeling the SEDs and correspond to the final 3D-*HST* data release.[13] Following van Dokkum et al. (2014), we applied a small correction to these stellar masses to take into account the difference between the total magnitude in the photometric catalog and the total magnitude implied by the Sérsic fit (see Taylor et al. 2010). On average, this correction is 1.03 ± 0.11. The central density is therefore calculated by numerically integrating the following equation:

$$\rho_1(r < 1\ \text{kpc}) = \frac{\int_0^{1\ \text{kpc}} \rho(r) r^2 dr}{\int_0^{\infty} \rho(r) r^2 dr} \frac{L_{\text{model}}}{L_{\text{phot}}} \frac{M_{\text{phot}}}{\frac{4}{3}\pi (1\ \text{kpc})^3}, \quad (1)$$

where L_{phot} is the total aperture-corrected luminosity of the galaxy from the 3D-*HST* catalogs in the filter corresponding to the Sérsic profile measurement (e.g., J_{F125W} or H_{F160W}). L_{model} is the total luminosity as measured from integrating the best-fit Sérsic profile. In 10% of the cases, the numerical integration does not converge and these unreliable measurements are removed from the subsequent analysis. We find that these galaxies generally have Gaussian profiles with $n = 0.45 \pm 0.14$, larger than average sizes with $r_e = 3.4 \pm 1.5$ kpc, and low stellar masses within $\lesssim$0.5 dex of the stellar mass limits; these galaxies represent precisely the population one might expect to fail. While we are effectively using the same formalism as van Dokkum et al. (2014), who derived the "core" mass within the central 1 kpc, we instead parameterized the central density and circular velocity within 1 kpc to facilitate comparisons to earlier results by Franx et al. (2008). We note that these derived parameters are essentially equivalent, modulo constant factors, where $M_1 \propto \rho_1 \propto v_{\text{circ},1}^2$.

Uncertainties in ρ_1 will originate from how well we can measure r_e and n for each individual galaxy, and to first order, this uncertainty depends on the signal-to-noise ratio (S/N). Using the CANDELS-wide H_{F160W} imaging, van der Wel et al. (2012) showed that the parameter r_e can be inferred with a systematic uncertainty of 10% or better for galaxies brighter than $H_{\text{F160W}} \sim 24$, whereas n can be measured at the same level of accuracy for galaxies brighter than $H_{\text{F160W}} \sim 23$. We adopted the corresponding limits in stellar mass for reliable r_e for the subsequent analysis. We note, however, that these stellar mass limits are roughly 0.5 dex lower than those for reliable n, as n is more challenging to constrain. We return to this issue in Section 4.3.

To quantify the errors on the central density, we performed 50 bootstrap simulations of this numerical integration, perturbing r_e by pseudo-random offsets drawn from a Gaussian distribution with a standard deviation equal to the respective 1σ errors, as calculated by van der Wel et al. (2012). As the errors on r_e are strongly correlated with both n and magnitude/stellar mass (Häussler et al. 2007; Guo et al. 2009; Bruce et al. 2012; van der Wel et al. 2012), we used the following equations, $\Delta(\log r_e) = -0.25\Delta(\log M_\star))$ and $\Delta(\log n) = -0.27\Delta(\log M_\star))$ (estimated from Figure 7 in van der Wel et al. 2012), to derive the offsets in n and $M_\star$ given $\Delta(\log r_e)$ for each bootstrap iteration of the numerical integration. The width of the resulting distribution of central densities is taken as the error on each individual measurement of ρ_1. The error on the average central density for each bin is then the square root of the sum of the errors in quadrature divided by the number of galaxies in the bin.

2.5. Central Circular Velocity

When we balance the gravitational force acting on the mass enclosed within the central 1 kpc with the centrifugal force, assuming spherical symmetry, the circular velocity of a test particle at radius $r = 1$ kpc is

$$v_{\text{circ},1}(r < 1\ \text{kpc}) = \sqrt{\frac{GM(r < 1\ \text{kpc})}{1\ \text{kpc}}} = \sqrt{\frac{4}{3}\pi G \rho_1}, \quad (2)$$

where G is the gravitational constant and equal to 4.302×10^{-6} kpc $M_\odot^{-1}$ $(\text{km s}^{-1})^2$, and the stellar mass enclosed within the central 1 kpc sphere is determined from Equation (1). The central circular velocity is a factor of $\sqrt{2}$ greater than the velocity dispersion, which both Franx et al. (2008) and van

[13] http://3dhst.research.yale.edu/Data.php

Dokkum et al. (2015) have studied. We again caution that we must be careful to test that the results presented here are not driven by flat galaxies, which deviate from the assumption of spherical symmetry. We return to this issue in Section 4.2.

3. The Dependence of Star Formation Rate on Galaxy Size

3.1. How Does Star Formation Rate Depend on Galaxy Size?

In Figure 1 we present the rest-frame 5000 Å size of galaxies as a function of their stellar mass in three redshift intervals, $0.5 < z < 1.0$, $1.0 < z < 1.5$, and $1.5 < z < 2.5$. The data are grouped into 0.2 dex bins of logarithmic stellar mass and size. The size of the symbol represents the number of galaxies that populate that area in parameter space. The symbols are color-coded by the sSFR derived from the UV+IR median stacking analysis, with open symbols signifying upper limits. While all galaxies are included in the left panels, the middle and right panels are separated into the star-forming and quiescent populations as determined from rest-frame $U - V$ and $V - J$ colors. The middle and right panels of Figure 1 additionally show the size–mass contours in grayscale of the opposite population, quiescent and star-forming, respectively. We alternatively show a similar figure in the Appendix, which is instead color-coded by the deviation from the average log(SFR)–log($M_\star$) relation from Whitaker et al. (2014).

For the overall galaxy population (Figure 1, left), galaxies with smaller sizes at fixed stellar mass are forming stars at lower rates. We confirm the earlier results of van der Wel et al. (2014) and numerous others, who showed that the compact sizes of more massive quiescent galaxies are offset from the average size of star-forming galaxies by factors of approximately four at fixed stellar mass at least out to $z \sim 2.5$. Here we show that these compact galaxies indeed have low sSFRs (see also van Dokkum et al. 2015). As Fumagalli et al. (2014) pointed out, the true SFRs of quiescent galaxies may be even lower as the mid-IR flux density can originate from processes unrelated to ongoing star formation, such as cirrus dust heated by old stellar populations and circumstellar dust. The UV+IR SFRs derived for quiescent galaxies here are therefore very likely upper limits (right panels in Figure 1), with the effect setting in for SFRs derived at 24 μm with log sSFR < -10 yr^{-1} (e.g., Utomo et al. 2014). Accounting for the overestimation of the quiescent SFRs by treating the SFRs measured for log sSFR < -10 yr^{-1} as upper limits will only serve to accentuate the trends between galaxy size and SFR for the overall population.

In the rightmost panels of Figure 1, we see a flattening of the galaxy size–mass relation for quiescent galaxies at low stellar masses ($<10^{10}\,M_\odot$), similar to Cappellari et al. (2013) and Norris et al. (2014). This is most evident at $0.5 < z < 1.0$, where the stellar mass limits imposed by the structural measurements extend to $10^9\,M_\odot$. This flattening is probably not the result of an inability to measure small galaxy sizes that are due to the *HST* resolution limit within the mass/magnitude limits we adopted because van der Wel et al. (2012) showed that the sizes of small galaxies are not overestimated if they have a sufficiently high S/N. van der Wel et al. (2012) compared measurements from data with different depths (CANDELS deep versus wide), as well as simulated Sérsic profiles. The former analysis will quantify random errors and take into account that galaxies are not necessarily well described by Sérsic profiles; the latter analysis is useful for understanding systematic effects under the assumption that galaxies are well described by Sérsic profiles. There is strong evidence suggesting that the Sérsic indices we measure from CANDELS data are reliable, as we are reliable, as we are not missing light at large radii due to lack of depth (van der Wel et al. 2008; Szomoru et al. 2010, 2013). These low-mass quiescent galaxies therefore appear to have sizes similar to the bulk of the star-forming population at that epoch, as well as slightly higher sSFRs than more massive quenched galaxies. Simulations also show this flattening in the slope of the size–mass relation at stellar masses below $10^{10}\,M_\odot$ in quiescent galaxies (e.g., Shankar et al. 2014; Furlong et al. 2017). These results indicate a more gradual quenching of star formation, perhaps due to a depleted gas supply. These trends are most likely not driven by environmental effects: results from Huertas-Company et al. (2013) showed no significant environmental dependence of the sizes of central and satellite quiescent galaxies at fixed stellar mass at $z \sim 0$.

3.2. At What Galaxy Size Scale Does Most Star Formation Occur?

With the present observations, it is interesting to consider on what galaxy size scale most of the stars in the universe form. In Figure 2 the symbol size represents the product of the median sSFR for that bin with the number of galaxies. A symbol can be small either because there are few galaxies that populate that parameter space and/or because those galaxies are not forming very many new stars on average. As we take the median when deriving the UV+IR SFRs, star-forming galaxies far above the main ridgeline of the star formation sequence will not dominate the stacks. The black line demarcates the 50th percentile, signifying the size scale at which half of the star formation for a given stellar mass occurs. The gray shaded region then shows the 25th and 75th percentile range, encompassing half of the star formation in the universe. These percentiles were determined by rank ordering the individual galaxies for a given stellar mass bin by size and summing their sSFRs until reaching 25%, 50%, and 75% of the total sSFR for that given stellar mass bin. This assumes that each galaxy within a bin is well represented by the median stacked sSFR, as the individual galaxies adopt this median value. We see that 50% of stars are formed in galaxies with sizes within ± 0.13 dex from the average star-forming size–mass relation, which is shown as the solid blue line from van der Wel et al. (2014) for comparison. As the mean is a more physically relevant metric, we repeated the above analysis from the mean stacks of 24 μm, finding a marginally wider spread of ± 0.14 dex. This width of 0.26 dex (0.28 dex for the mean) is of similar order to the 1σ intrinsic scatter of the size–mass relation (see Figure 6(c) in van der Wel et al. 2014). Most of the stars in the universe are formed in star-forming galaxies with typical sizes.

While we find that among the overall galaxy population most of the star formation occurs within a narrow range of sizes, we can further explore whether there is any dependence on the SFR *within* the star-forming population. In the following section, we isolate these star-forming galaxies based on their rest-frame $U - V$ and $V - J$ colors (see Figure 26 in Skelton et al. 2014).

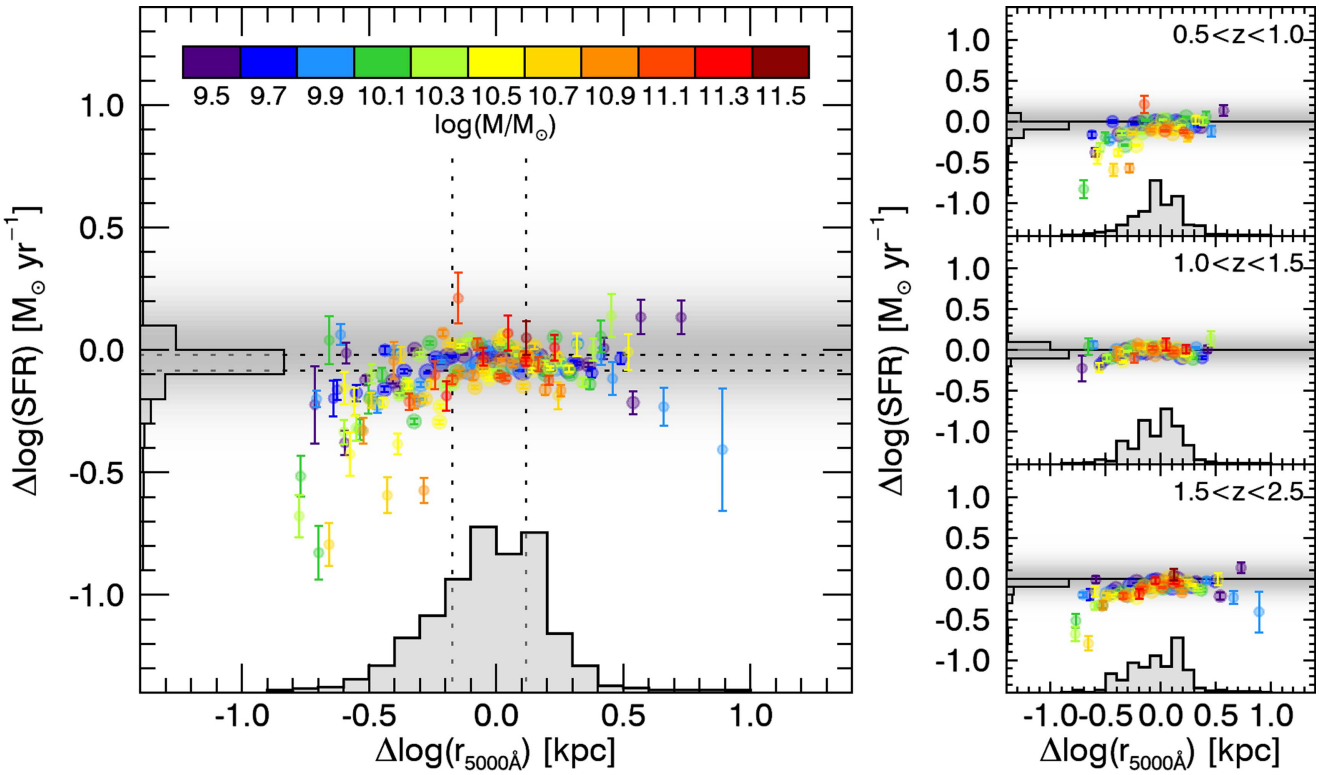

Figure 3. Residual observed UV+IR star formation rate as a function of residual galaxy size from a stacking analysis across the size–mass plane in 0.2 dex bins for UVJ-selected star-forming galaxies. Given the average redshift and stellar mass of each measurement, the well-known correlations between log(SFR)–log($M_\star$) and log (r_e)–log($M_\star$) are subtracted to yield the residual values. Although the majority of galaxies show little dependence on galaxy size, we see that intermediate-mass (log ($M_\star/M_\odot$) $\sim$ 10.0–10.6) compact galaxies have star formation rates lower by >0.5 dex below the average relations. The left panel compiles all redshifts from $z = 0.5$ to $z = 2.5$, while the right three panels break down the measurements by redshift bin. The histogram shows the galaxy size distribution with the average relation subtracted. The grayscale horizontal band indicates the observed 0.3 dex scatter in the star formation sequence for reference, with a Gaussian transparency distribution, and the dotted lines mark the 0.2 dex typical scatter in the observed size–mass relation.

3.3. Do We See Variations in Star Formation with Galaxy Size within the Star-forming Population Alone?

When solely selecting actively star-forming galaxies based on their rest-frame colors (middle panels in Figure 1), the dependence of the median sSFR of a galaxy on size is far less pronounced than for the overall galaxy population (left panels). To first order, for any given stellar mass, larger star-forming galaxies have the same sSFR as smaller star-forming galaxies within <0.2 dex. We start to see deviations from this trend at the highest stellar masses and lowest redshift interval. This is most likely related to the observed flattening in the slope of the star formation sequence toward later times for galaxies more massive than $\sim 10^{10.5}$ $M_\odot$ (e.g., Whitaker et al. 2014; Lee et al. 2015), and the correlation between this flattening and Sérsic index (Whitaker et al. 2015). We note that the trends between the size–mass plane and sSFR for star-forming galaxies agree nicely with those at $z = 0$ presented in Figure 14 of Omand et al. (2014).

In order to better quantify the dependence of the average SFR on galaxy size, we must first remove the well-known trends with stellar mass and redshift. As detailed in the Appendix, we reproduce the size–mass relation first presented in Figure 1, but instead color-code by Δlog(SFR) (Figure 15). Next, we use the size–mass relation of van der Wel et al. (2014) to determine Δlog(r_e) for each 0.2 dex bin in stellar mass and size. Figure 3 presents this residual relation between the average SFR and rest-frame 5000 Å galaxy size for star-forming galaxies alone. The grayscale demarcates the typical observed 0.3 dex scatter in the star formation sequence (e.g., Rodighiero et al. 2011; Whitaker et al. 2012b; Speagle et al. 2014), where the transparency is defined by a Gaussian distribution.[14] As each data point reflects one of the original 0.2 dex bins in size and mass, we do not expect a scatter plot. Even with our stacking analysis, however, we would be sensitive to an overall correlation between scatter about the star formation sequence and scatter about the size–mass relation.

When taking into account the number of galaxies that go into each stack, we generate histograms of the original data by adopting the median stacked SFR from each bin together with the input size and stellar mass distributions (shown in gray on the x- and y-axes). When we split the data into quartiles in Δlog (SFR) (y-axis histogram), we find only a weak dependence on size; Δlog(r_e) for galaxies in the highest quartile are 0.27 ± 0.06 dex larger than galaxies in the lowest quartile. In other words, we see that the residual median SFRs of the majority of galaxies show little dependence on galaxy size (see also J. Fang et al. 2017, in preparation). If we instead split the quartiles based on Δlog(r_e) (x-axis histogram), we similarly find a trend only among the smallest galaxies where Δlog (SFR) is 0.11 ± 0.02 dex lower that of the largest galaxy quartile. This population of compact "fading" star-forming galaxies is also clearly visible in the middle panels of Figure 15.

[14] The y-axis is measured from a stacking analysis, therefore we do not recover the intrinsic scatter in the SFR.

Using spatially resolved maps of Hα for star-forming galaxies at $z \sim 1$ in the 3D-*HST* survey, Nelson et al. (2016a) found that Hα is enhanced at all radii above the main ridgeline of the log(SFR)–log($M_\star$) plane and depressed at all radii below. This suggests that the physical processes driving the rate of star formation acts throughout the entirety of galaxy disks. Taking these results at face value with the present analysis, this supports the idea that average galaxies follow "parallel-tracks" (van Dokkum et al. 2015, see Section 4.2 for further discussion). We note that this picture is complicated by the presence of large amounts of dust (and associated cold molecular gas) and apparent gradients thereof (e.g., Tacconi et al. 2010, 2013; Genzel et al. 2015; Simpson et al. 2015; Tadaki et al. 2015; Nelson et al. 2016b), as well as potential systematic uncertainties introduced by the stacking methods employed. While results from Morishita et al. (2015) demonstrate that the stellar mass density profiles do not appear to depend strongly on any potential color gradients, other studies have found spatial variations in mass-to-light ratios to be important (e.g., Wuyts et al. 2012; Lang et al. 2014). We discuss this issue further in Section 4.2.

We have performed several tests in order to explore if the lack of trend between (s)SFR and galaxy size is driven by either the relatively large redshift bins or the adopted SFR indicator. When we assume that the sSFR of any given galaxy is independent of the size, we can use the same parent sample redshift distribution and the well-observed average relation between log(SFR)–log($M_\star$) to randomly assign each galaxy a size from the van der Wel et al. (2014) size–mass relation. We find that we can reproduce all observed trends, shy of the lower envelope of compact fading star-forming galaxies. The large redshift bins therefore do not affect the conclusions of this paper.

The UV+IR total SFRs probe star formation timescales of order 100 Myr. When instead considering the Hα SFR indicator, which is sensitive to shorter timescales on the order of 10 Myr, we find the same trends among star-forming galaxies in Figure 4. For this test, we used the Hα emission line fluxes from the 3D-*HST* survey in the two lowest redshift bins and corrected for dust attenuation from the best-fit A_V from the SED. Even though this dust correction is somewhat uncertain (see Whitaker et al. 2014), we are probably underestimating the dust attenuation, which could enhance the trends between galaxy size and sSFR slightly. However, from this test we can conclude that the general independence of SFR and galaxy size is most likely not sensitive to the timescale on which the SFR is probed.

The notable exception to the lack of dependence on sSFR are galaxies with intermediate stellar masses ($\log(M_\star/M_\odot) \sim$ 10.0–10.6) and compact sizes ($r_e < 2$ kpc). These massive compact galaxies have significantly lower SFRs than the bulk population of star-forming galaxies. They may be in the process of fading to join the quiescent population (see also Yano et al. 2016). Larger statistical samples and/or deeper 24 μm observations are required to further improve the uncertainty in the SFRs presented here. Nonetheless, we see evidence for an interesting trend between the SFRs and sizes of intermediate-mass compact star-forming galaxies.

Now that we have confirmed the dichotomy between the sizes of quiescent and star-forming galaxies (Section 3.1), with most of the star formation occurring within a narrow range of sizes (Section 3.2), we additionally show that there is little dependence of sSFR on size within the star-forming galaxies alone. Taking these three points together, this suggests an abrupt change in SFR after a galaxy attains a particular structure. In the next section, we investigate how well various galaxy structure parameters can uniquely predict this decrease in sSFR.

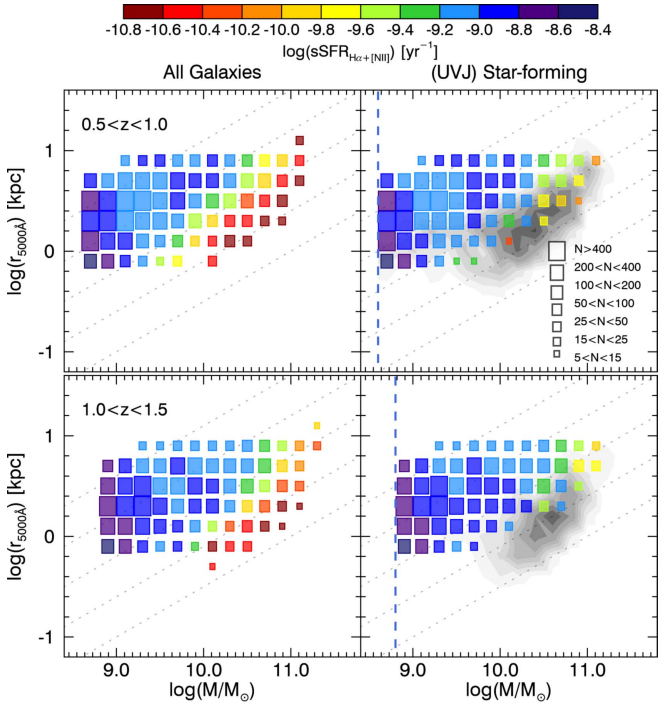

Figure 4. When considering the dust-corrected Hα sSFR, we find the same general trends as the UV+IR SFR among the overall galaxy population: large galaxies have higher sSFRs than smaller galaxies at fixed stellar mass. Similarly, we find the same lower envelope of compact star-forming galaxies with depressed sSFRs.

4. Predicting Quiescence

The several competing theories put forth to explain the simultaneous evolution of the structures of quiescent and star-forming galaxy populations across cosmic time predict in each case how galaxies are expected to grow in stellar mass with respect to their structures. Barro et al. (2015) postulated that the distribution of massive galaxies form an "L-shaped track" comprised of the two fundamental physical processes of compaction and quenching. Galaxies will continue to gradually grow inside-out (e.g., Nelson et al. 2016a) until they reach a strong phase of core growth. Also known as compaction, this is a rapid period in which star-forming galaxies become structurally similar to quiescent galaxies, growing in central density (also increasing their core-to-total mass and Sérsic indices, and decreasing their size) (see Dekel & Burkert 2014; Zolotov et al. 2015). Quenching occurs when these compact star-forming galaxies reach a central density threshold.

On the other hand, the "parallel tracks" model by van Dokkum et al. (2015)[15] instead suggests that galaxies follow an inside-out growth track in the size–mass plane, where the stellar mass is gradually increased within a fixed physical radius and galaxies quench when they reach a stellar density or

[15] The probable progenitors of galaxies are predicted in this model by tracing toward lower stellar masses and smaller sizes in the size–mass plane, hence following "parallel tracks" for a given galaxy size at fixed stellar mass.

velocity dispersion threshold. The relatively small observed scatter in the size–mass relation (van der Wel et al. 2014) and the star formation sequence (Whitaker et al. 2012b) support this idea of a more gradual growth of galaxies.

Regardless of the timescale defining the build-up of the central mass concentration and the transition to quiescence, the common denominator between these various physical mechanisms is the existence of a threshold in either stellar density or velocity dispersion. We first explore if galaxy size or Sérsic index alone could predict quiescence in Section 4.1. Next, we perform a detailed analysis of the dependence of the stellar mass surface density and central density on sSFR in Section 4.2, parameterizing these correlations with broken power-law fits in Section 4.3. Finally, we define quiescence and the redshift evolution in the quenching threshold in Section 4.4.

4.1. Which Role Do Galaxy Size and Sérsic Index Play in Predicting Quiescence?

From the present analysis, there are two interesting points regarding the ability to predict when a galaxy will quench: (1) compact galaxies have lower sSFRs on average (Section 3.1), and (2) most stars form in galaxies with typical (larger) sizes for their given total stellar mass (Section 3.2). If a galaxy is observed to have a compact size for the given total stellar mass, does this uniquely predict that it will be quenched? We can recast the information in Figure 1 to instead plot the sSFR as a function of $\Delta\log(r_e)$, or the deviation in size from the average size–mass relation (see Appendix for more details). In Figure 5 we show that galaxies with lower sSFRs are smaller than average with red rest-frame $U-V$ colors. However, it is important to note that a population of similarly compact galaxies with more typical sSFRs also exists. This emphasizes that for a given stellar mass, galaxy size alone cannot predict quiescence.

We next consider the Sérsic index n: in the case of "morphological quenching" (e.g., Martig et al. 2009, 2013; Genzel et al. 2014), a galaxy will quench once it builds up a significantly massive bulge, as indicated observationally by a high Sérsic index n (e.g., Bruce et al. 2014). As an earlier study by Whitaker et al. (2015) did not explicitly present the dependence of sSFR on n in the same manner as the present analysis, we show this in Figure 6, color-coded by the average rest-frame $U-V$ color. While high n generally indicates lower sSFR, n is not a unique predictor either; galaxies with high n (bulge-dominated) exhibit a broad range of sSFRs that is strongly correlated with their rest-frame $U-V$ colors (see also discussion in Bell et al. 2012). The trends present in Figure 6 are striking, with important implications for the derived slope and scatter of the star formation sequence. With these same data, Whitaker et al. (2015) showed that the slope is on the order of unity for disk-like galaxies, equivalent to a constant sSFR. On the other hand, galaxies with $n > 2$ (implying more dominant bulges and higher central densities) have significantly lower sSFRs than the main ridgeline of the star formation sequence. Brennan et al. (2015) presented a schematic diagram of how the various physical mechanisms could move galaxies around the sSFR–n plane, accounting for dry and wet mergers, disk instabilities, galaxy harassment, AGN feedback, and other slow gas-depletion processes. However, the relevant result from the present data is that both galaxy size and n alone are insufficient to isolate quiescent galaxies with low sSFRs.

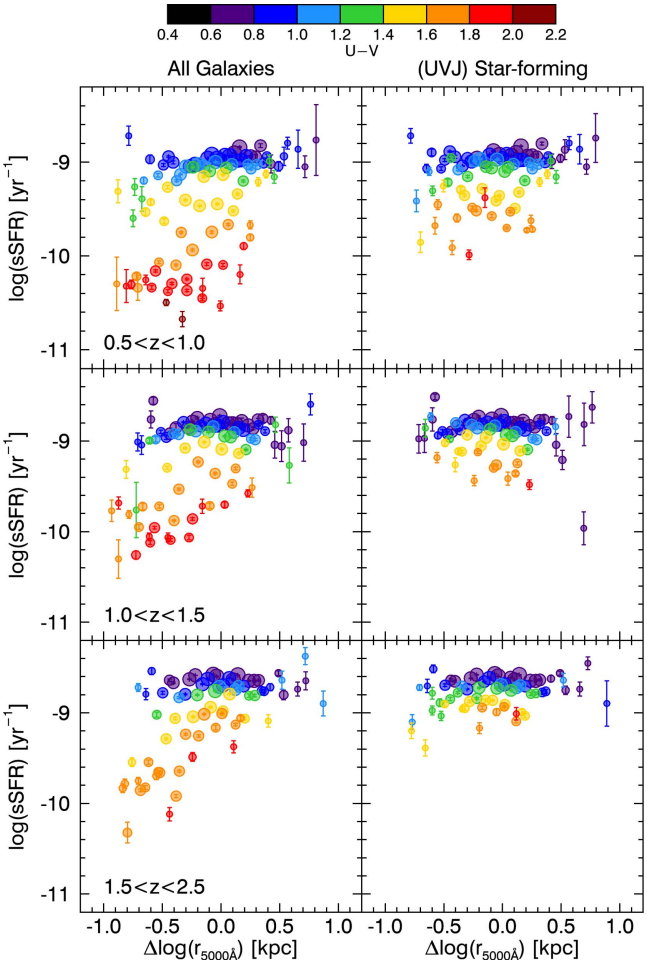

Figure 5. Deviation of the logarithmic rest-frame 5000 Å galaxy size from the average size–mass relation binned by 0.2 dex in mass and size and color-coded by rest-frame $U-V$ color shows correlations with the median sSFR and rest-frame color. Negative values indicate galaxies that are more compact than average for their given stellar mass. The left panels show all galaxies, while the right panels show UVJ-selected star-forming galaxies only. The most compact galaxies have the lowest sSFRs and reddest rest-frame colors, but there also exist similarly compact galaxies with high sSFRs and blue rest-frame $U-V$ colors.

The stellar mass density profile of a galaxy is defined by both the effective radius and the Sérsic index n of a galaxy. The combination of these two parameters may therefore be more powerful than either parameter alone. Figure 7 demonstrates the strong correlation between galaxy size and Sérsic index at fixed stellar mass. In this figure, we selected a small number of galaxies from the parent sample such that they inhabit a narrow range in stellar mass of $10.45 < \log(M/M_{\odot}) < 10.50$ at $1.0 < z < 1.5$. The galaxies are color-coded by their deprojected central density within a fixed physical radius of 1 kpc, as derived in Section 2.4. We show in Figure 7 that the stellar mass density within the central 1 kpc of these galaxies is strongly correlated with both size and Sérsic index. In the following sections, we explore if this stellar mass density is the most reliable predictor of quiescence, compared to stellar mass, r_e, or n alone.

4.2. Does a Central Density or Circular Velocity Threshold Uniquely Predict Quiescence?

We performed a similar analysis as in Figure 1, but instead derived median stacked UV+IR (s)SFRs in 0.2 dex bins of

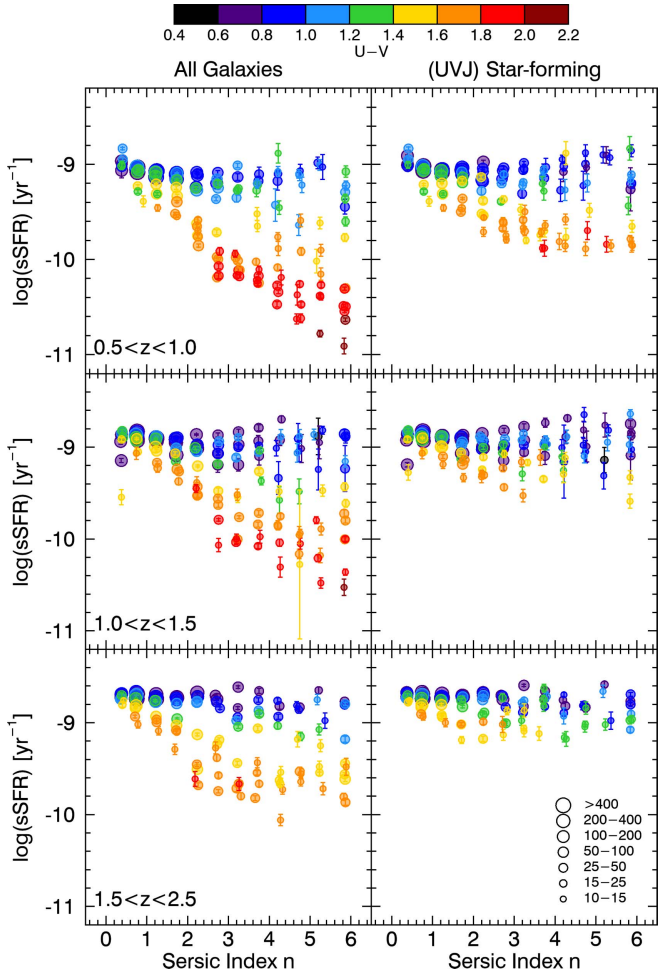

Figure 6. Average Sérsic index n for all galaxies (left) and UVJ-selected star-forming galaxies (right) is well correlated with the median sSFR for a given rest-frame $U - V$ colors across all redshifts probed here. Quantities are derived for galaxies stacked in the n-log($M_\star$) plane, with 0.2 dex bins for log($M_\star$) and 0.5 width bins in n. As there is no universal trend, this implies that although n is a good predictor of quiescence, it is not a sufficient condition to predict a low sSFR. The implications of these results on the slope and scatter of the star formation sequence are presented in Whitaker et al. (2015).

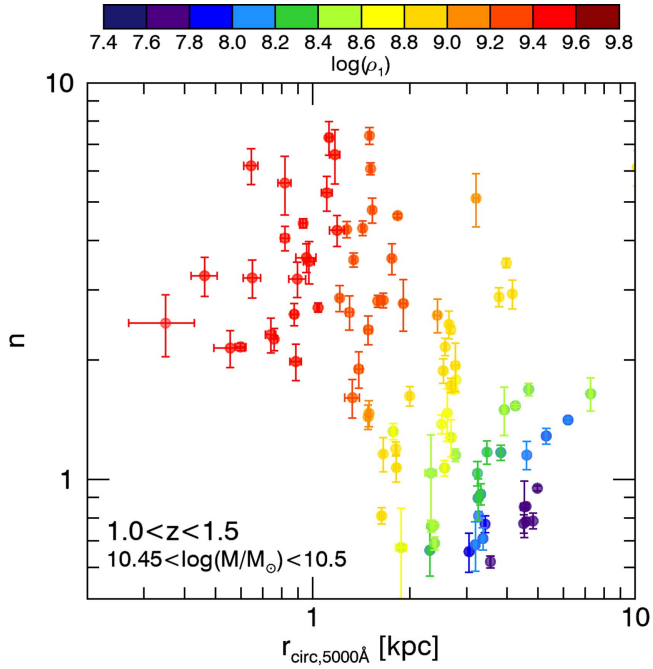

Figure 7. Rest-frame 5000 Å size of a galaxy is strongly correlated with the measured Sérsic index n, when selecting in a narrow range of stellar mass (selected to be $10.45 < \log(M/M_\odot) < 10.5$ for demonstration purposes only). The color-coding indicates the central density within a physical radius of 1 kpc for the individual galaxies: small galaxies with high n have high central densities, while larger galaxies with low n have lower central densities.

logarithmic stellar mass and stellar mass surface density (log(Σ_e); Figure 8) and central stellar density (log(ρ_1); Figure 9) in three redshift intervals, $0.5 < z < 1.0$, $1.0 < z < 1.5$, and $1.5 < z < 2.5$. A similar bootstrap analysis on the stacked IR SFRs was performed to derive uncertainties in the median values, as described in Section 2.4. These measured values were then recast as sSFRs as a function of log(Σ_e) and log(ρ_1) in the subsequent analysis. By using sSFR, we normalized the SFRs by stellar mass and probed an inverse timescale sensitive to the ages of the stellar populations. The individual measured values are shown in grayscale in Figures 8 and 9; the plume rising toward higher sSFR at the lowest densities, offset from the average relations, reflects the limits of the data on a galaxy-by-galaxy basis. Similarly, we see few individual 24 μm detections at the lowest sSFRs and highest densities. In both of these extreme parameter regimes, many of the individual galaxies remain undetected in the 24 μm imaging, necessitating the stacking analysis presented here.

Figure 8 shows a strong correlation between the median sSFRs from galaxy stacks and their stellar mass density within the effective radius. The result is strikingly different to that of Figures 5 and 6. For galaxies with low surface densities, the sSFR is roughly constant at a given epoch. On the other hand, we see a strong drop in the sSFR for galaxies with high densities. We observe these trends in all three redshift intervals, finding that the turnover in sSFR at higher densities is stronger for quiescent and star-forming galaxies together than for star-forming galaxies alone. As the majority of massive galaxies are quiescent (e.g., Muzzin et al. 2013) and have more centrally concentrated stellar mass profiles (e.g., Bell et al. 2012), they will preferentially pull down the median sSFR at the highest densities. If we instead consider the central density, which is derived from the deprojected stellar mass within a 1 kpc radius sphere, we see that the trend remains essentially the same shape but the scatter is significantly reduced in Figure 9. The offset in stellar density when comparing the solid and dashed black lines in Figure 8 results from the implicit difference between the stellar mass enclosed within the central 1 kpc as compared to the effective radius. We have already accounted here for the constant factor of 0.12 dex introduced during the deprojection from a sphere to a circle. While the trend in ΔSFR–$\Delta\Sigma_1$ from Barro et al. (2015) is coined an "L-track," we show the more gradual evolution with remarkably small scatter in sSFR with increasing central density when not correcting for stellar mass dependence, which also evolves with redshift, as we demonstrate below. These results are in good quantitative agreement with B. Lee et al. (2017, in preparation), who perform a similar analysis, but instead employ SFR indicators from SED fitting using flexible star formation histories.

Our results agree qualitatively with that of Woo et al. (2015) at $z = 0$, who showed that SDSS central galaxies with higher central surface densities have lower sSFR. It is somewhat challenging to directly compare the $z = 0$ results with the

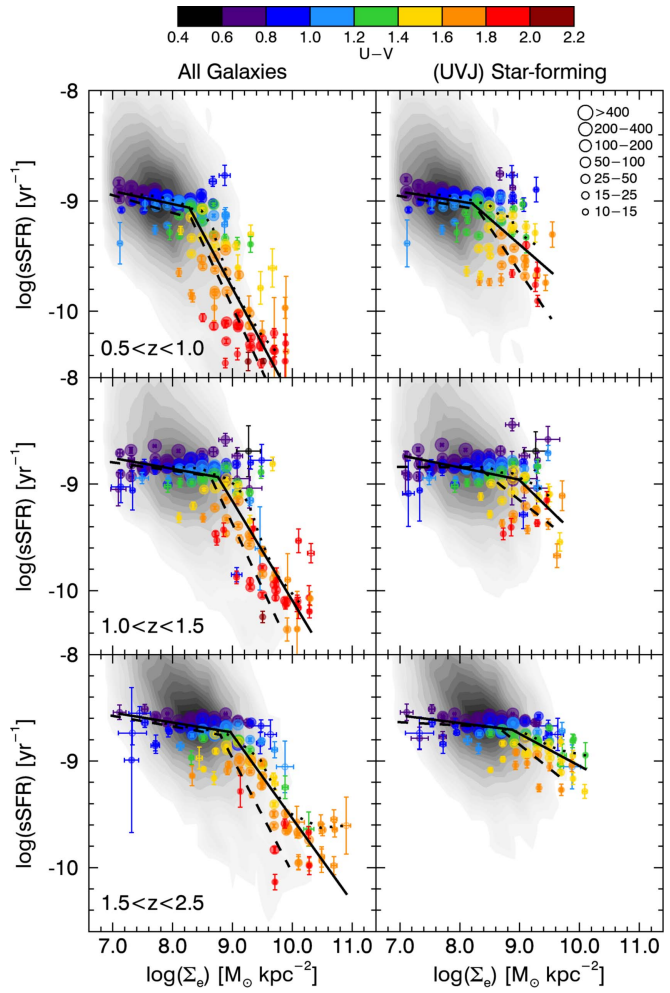

Figure 8. We show the correlation between the median sSFR and surface density of all galaxies (left) and UVJ-selected star-forming galaxies (right), color-coded by their average rest-frame $U - V$ colors. The sSFR is calculated here within 0.2 dex bins across the log(Σ_e)–log($M_\star$) plane, with the grayscale showing the contours for the overall galaxy population with individual 24 μm detections. While there is considerable scatter, especially among the more compact galaxies, there is a clear trend for a roughly constant sSFR for (blue) galaxies with surface densities lower than log(Σ_e) < 9 $M_\odot$ kpc^{-2} and a drop off in sSFR for (red) galaxies with higher surface densities. The dotted line is the running median. The solid black line is a broken power-law fit to the data, and the dashed line is the log(sSFR)–log(Σ_1) relation adapted from Figure 9, where log(Σ_1) = log(ρ_1)–log(4/3).

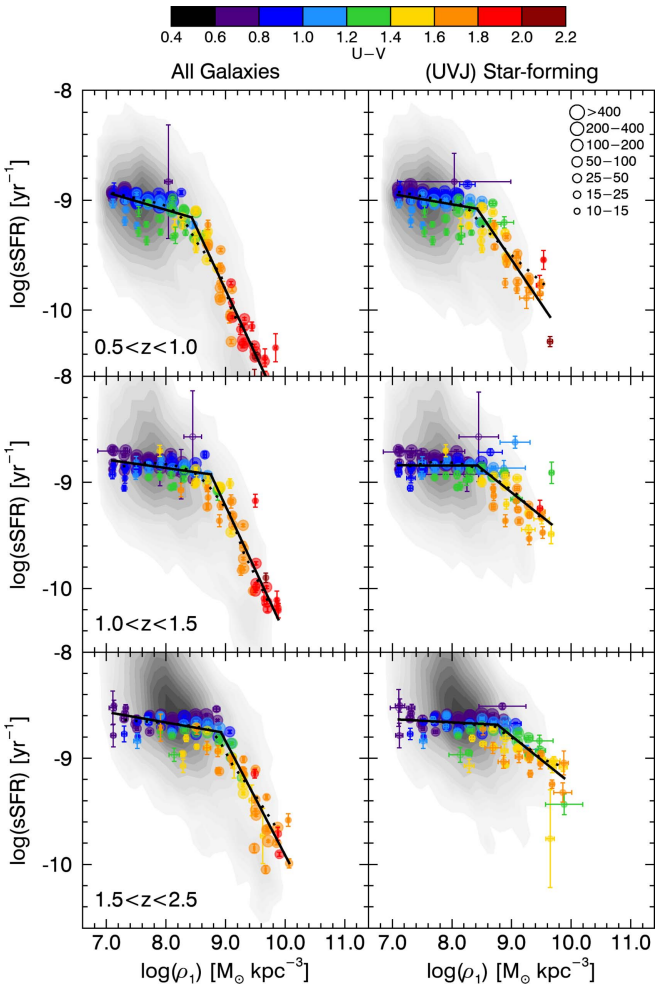

Figure 9. Similar to Figure 8, we now show the correlation between the median sSFR and central density, $\rho_1(r < 1$ kpc), for all galaxies (left) and UVJ-selected star-forming galaxies (right). The data are split into three redshift bins and color-coded by the average rest-frame $U - V$ colors. The sSFR is calculated here within 0.2 dex bins across the log(ρ_1)–log($M_\star$) plane. It is striking that the correlation between median sSFR and central density within 1 kpc is remarkably tighter than that with surface density as determined from the effective radius in Figure 8. Although the trends are similar, the scatter among the measurements decreases significantly when considering the central density of galaxies.

present analysis, as they separated their sample by stellar mass. In Figure 10 we isolate galaxies with log($M_\star/M_\odot$) $\geqslant$ 10.6 for both stellar surface mass density (left panel) and central surface density (right panel). To facilitate a direct comparison, we convert the central density to surface density here by applying an offset of 0.12 dex, corresponding to the equivalent difference in constants (see Equation (1)). While we only show the one redshift epoch, $0.5 < z < 1.0$, that has the largest dynamic range, we find similar trends at higher redshifts. We see that our measurements for the most massive galaxies span over two decades in stellar mass central surface density and almost two decades in sSFR. For similar stellar masses in Woo et al. (2015), the evolution in central surface density at $z = 0$ is significantly less pronounced, on the order of <0.5 dex. When considering where the most massive galaxies reside in the log (sSFR)–log(Σ_e) plane in the left panel of Figure 10, we see that they preferentially have lower sSFRs relative to the average relation, and thereby their less massive counterparts. Intriguingly, we no longer see this stellar mass dependence when instead considering central density (right panel, Figure 10).

The earlier results of Lang et al. (2014) showed that the bulge mass together with the bulge-to-total ratio (or n) correlates most strongly with the degree of quiescence. This implies that the central mass concentration is a key factor in quenching. Here we explicitly consider the density within the central 1 kpc out to $z = 2.5$ and demonstrate that it is indeed a remarkably clean tracer of the median sSFR of galaxies. Although we show that ρ_1 tracks the median dependence of sSFR on structure best, it may be that galaxies at a given ρ_1 exhibit a relatively broad range in intrinsic sSFRs. Given the nature of the stacking analysis employed here, we cannot further study the intrinsic scatter in this relation. Regardless, these results do confirm the low-redshift study by Teimoorinia et al. (2016), who used a novel technique to rank the relative importance of SDSS central galaxy properties in the process of quenching star formation. Similar to our conclusions,

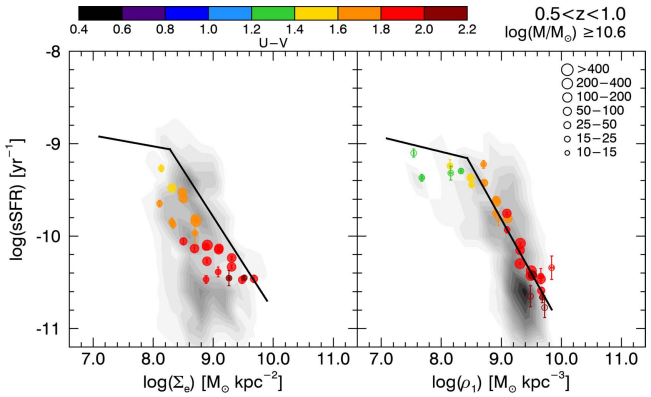

Figure 10. This figure replicates the top left panel from Figure 8 (left) and Figure 9 (right), but only showing the stacks of massive galaxies with log $(M/M_{\odot}) \geqslant 10.6$. The data are grouped into 0.2 dex bins of stellar mass and log (Σ_e) or log(ρ_1), and color-coded by the average rest-frame $U - V$ color. While the most massive galaxies lie systematically below the average log(sSFR)–log (Σ_e) relation (left), we do not see any such offset when instead considering the central surface density within 1 kpc (right). The grayscale shows the contours for the massive galaxies with individual 24 μm detections. Open symbols represent the 1σ upper limit in the measured sSFR.

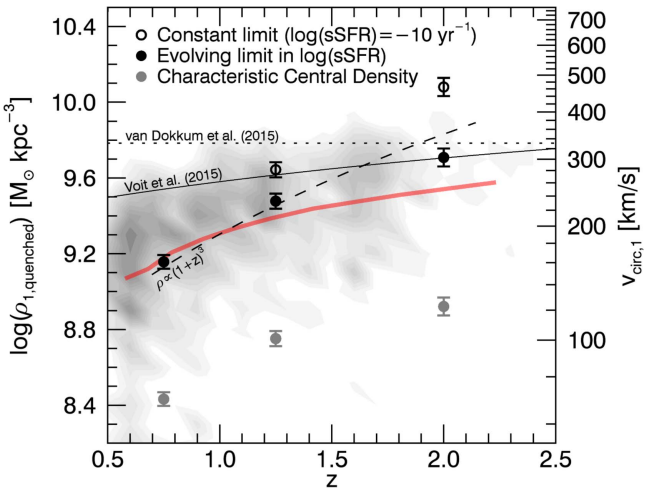

Figure 11. We find a strong evolution in the central density threshold for quenching. When we define a galaxy as quenched when log (sSFR) < -10 yr^{-1}, the corresponding central density measured from Figure 9, log$(\rho_{1,\mathrm{quenched}})$, is significantly higher at earlier times (open circles). We find a similar trend when we instead define quenching to occur when galaxies have sSFRs 1 dex below the average observed sSFR for low-mass galaxies (filled circles; overlapping by definition at $z = 0.75$). The gray filled circles indicate the characteristic density, log$(\rho_{1,\mathrm{char}})$, marking the turnover in the broken power-law fit. The grayscale shows the central densities measured for quiescent galaxies at analogous epochs, where the red line marks the running median of the quiescent population; the median central density of the quiescent population lies just below the quenching threshold at $z > 1$. The dashed line indicates the expected cosmological evolution in density normalized at $z = 0.5$, where $\rho \propto (1+z)^3$. We also show the equivalent central circular velocity on the right axis, where $v_{\mathrm{circ},1} \propto \sqrt{\rho_1}$. The dotted line is the assumed constant threshold in velocity dispersion above which galaxies at $1.5 < z < 3.0$ quench from van Dokkum et al. (2015). The thin black line is the predicted quenching threshold from Voit et al. (2015), normalized to 300 km s^{-1} at $z = 2$.

Teimoorinia et al. (2016) find that central velocity dispersion and/or central stellar mass concentration are excellent predictors of the cessation of star formation.

The present analysis rests on the assumption that light traces mass (Sections 2.2 and 2.4). When accounting for any potential variations in mass-to-light ratios from either the star formation histories, ages, or dust across the galaxies, Wuyts et al. (2012) and Lang et al. (2014) showed that the stellar mass maps and profiles are generally smoother and more centrally concentrated than the profiles in rest-frame UV and optical light. Furthermore, the evidence is mounting for massive compact concentrations of gas and dust residing in a significant fraction of typical star-forming galaxies toward the high-mass end from high-resolution studies of the rest-frame UV/optical light (Guo et al. 2011, 2012; Wuyts et al. 2012; Szomoru et al. 2013; Boada et al. 2015; Tacchella et al. 2015b), as well as (sub) millimeter studies (Tacconi et al. 2013; Simpson et al. 2015; Tadaki et al. 2015). The highest stellar mass star-forming galaxies may be affected most severely, where we could be underestimating their central mass concentration. Preferentially underestimating the central densities and/or the SFRs (e.g., Nelson et al. 2016b) of the most massive star-forming galaxies could make the turnover in sSFR above the density threshold (falsely) steeper. Figure 10 demonstrates the dynamic range in central density that the most massive galaxies inhabit. Although the effects of variations in mass-to-light ratios are stronger toward higher stellar masses, the location of the break in the log(sSFR)–log(ρ_1) plane may not be affected severely as the vast majority of massive galaxies have central densities well above the turnover.

4.3. Broken Power-law Fits

We fit the log(sSFR)–log(Σ_e) relation in Figure 8 and log (sSFR)–log(ρ_1) relation in Figure 9 with broken power laws to independently quantify the behavior of galaxies above and below the characteristic values of Σ_e and ρ_1. The broken power law is parameterized as

$$\log(\mathrm{sSFR}) = a(\log(X) - b) + c, \quad (3)$$

where X equals either Σ_e or ρ_1. The slope a is roughly flat below the characteristic densities b (Figure 11), and steeply drops off above these characteristic values. Hereafter, these characteristic densities are notated as either $\Sigma_{e,\mathrm{char}}$ or $\rho_{1,\mathrm{char}}$. The best-fit parameters and their associated uncertainties are listed in Tables 1 and 2. We see that the best-fit power law is very similar between the log(sSFR)–log(ρ_1) relation in Figure 9 and that of log(sSFR)–log(Σ_e) relation in Figure 8. The best-fit log(sSFR)–log(Σ_1) relation is shown as a dashed line for reference in Figure 8, where log$(\Sigma_1) \equiv$ log(ρ_1)–log$(4/3)$. The main difference between these two measurements is that there is a significantly larger scatter among the average measured values of Σ_e, while ρ_1 (or Σ_1) shows remarkably little scatter.

In order to test that the trends we observe in Figure 9 are not driven by flat galaxies, where the deprojected central density may not be trustworthy given the assumptions, we repeated the analysis by removing all galaxies with $n < 2$. We find that the best-fit power laws for the entire sample are unchanged, although we are missing the vast majority of data points falling below log$(\rho_1) < 7.5$ $M_{\odot}$ kpc^{-3} where most galaxies are disks with low n. Furthermore, as the numerical integration to measure ρ_1 depends not only on the reliability of r_e but also n, we must test a more conservative stellar mass limit. If we remove all galaxies within 0.5 dex of the stellar mass limits, as required to ensure sufficient S/N for robust measurements of n for all galaxies, we find the best-fit power law fit to be statistically unchanged. We therefore assert that the observed

Table 1
Broken Power-law Fits: log(sSFR)–log(Σ_e)

	All Galaxies				UVJ Star-forming			
Redshift Range	a_{low}	a_{high}	b	c	a_{low}	a_{high}	b	c
$0.5 < z < 1.0$	-0.12 ± 0.04	-1.01 ± 0.03	8.28 ± 0.03	-9.06 ± 0.02	-0.09 ± 0.04	-0.47 ± 0.04	8.21 ± 0.07	-9.02 ± 0.02
$1.0 < z < 1.5$	-0.10 ± 0.03	-0.93 ± 0.05	8.76 ± 0.04	-8.93 ± 0.02	-0.12 ± 0.02	-0.55 ± 0.17	8.99 ± 0.12	-8.96 ± 0.03
$1.5 < z < 2.5$	-0.09 ± 0.03	-0.78 ± 0.04	8.97 ± 0.04	-8.73 ± 0.02	-0.07 ± 0.03	-0.30 ± 0.05	8.87 ± 0.11	-8.71 ± 0.02

Note. Broken power-law coefficients parameterizing the evolution of the log(sSFR)–log(Σ_e) relation from the median stacking analysis (Equation (3)). a_{low} signifies the best-fit slope for galaxies below the characteristic stellar surface mass density Σ_e, and a_{high} is the slope above this limit.

correlations in this analysis appear stable against systematic biases in the structural parameters.

4.4. Do We See Redshift Evolution of the Quenching Threshold in Central Density and Circular Velocity?

While the characteristic central density, $\rho_{1,char}$, marks a threshold above which galaxies become less efficient at forming new stars, it does not necessarily signal quiescence. We could simply define a galaxy to have reached quiescence when log (sSFR) $< -10\,\mathrm{yr}^{-1}$. Alternatively, a galaxy could be defined as quenched when it deviates significantly from the average star formation sequence at that cosmic epoch. This latter definition will result in an evolving limit in log(sSFR) with cosmic time. To that end, here we estimate the quenching limit in sSFR in one of two ways: (1) at a fixed limit of log(sSFR) $< -10\,\mathrm{yr}^{-1}$, and (2) for an evolving limit in log(sSFR) based on results presented in Whitaker et al. (2014). The critical central density for quenching, which we define to be $\rho_{1,quenched}$, is then taken to be the central density at these respective sSFR limits in Figure 9. For the purpose of this exercise, we only consider lower mass galaxies where the sSFR is roughly constant when calculating the evolving limit, ignoring the strong evolution in the turnover in sSFR at the massive end. When we assume that the average log(sSFR) equals -9.0, -8.8, and $-8.6\,\mathrm{yr}^{-1}$ at $0.5 < z < 1.0$, $1.0 < z < 1.5$, and $1.5 < z < 2.5$, respectively, an offset of 1 dex below the star formation sequence ($\sim 3\sigma$) reaches log (sSFR) $= -9.6\ \mathrm{yr}^{-1}$ at $z = 2$ and lower values at later times (log(sSFR) $= -10\,\mathrm{yr}^{-1}$ by $z = 0.75$). Barro et al. (2015) adopted a 0.7 dex offset below the star formation sequence, but they normalized at the massive end where there is an evolving turnover toward increasingly lower sSFRs relative to the lower mass population as redshift decreases.

Regardless of the adopted definition of quiescence, the average trends in Figure 11 indicate that the quenching threshold is almost a decade higher at $z \sim 2$ compared to $z \sim 0.7$. This implies that, on average, quiescent galaxies that quench at later times will have lower central densities and velocities. Furthermore, the quenching density as defined by a fixed offset from the average star formation sequence (and correspondingly evolving sSFR limit) has the same redshift evolution as the characteristic density (gray points in Figure 11).

We furthermore compared our results to density and velocity thresholds presented in the literature. After factoring out the stellar mass dependence of $\log(\Sigma_1)$, Barro et al. (2015) asserted that galaxies quench once they reach a central surface density of $\log(\Sigma_1) > 9.5\ M_\odot\,\mathrm{kpc}^{-2}$ (or $\log(\rho_1) > 9.38\ M_\odot\,\mathrm{kpc}^{-3}$, when accounting for the deprojection of a sphere of radius 1 kpc). This correction for the stellar mass dependence of $\log(\Sigma_1)$ accounts for the difference between the more gradual turnover in sSFR above the characteristic central density we observe here and the abrupt turnover in $\Delta\log(\Sigma_1)$ presented in Figure 7 of Barro et al. (2015). Perhaps unsurprisingly, the trends we observe in Figure 11 are close to the expected cosmological evolution of density, as $\rho \propto (1+z)^3$ (dashed line, normalized to the lowest redshift measurement). Similarly, as $v_{circ,1} \propto \sqrt{\rho}$, the central circular velocity scales as $(1+z)^{3/2}$. As the central circular velocity is directly proportional to the central density (see Section 2.5), we show the corresponding values of $v_{circ,1}$ in the right axis of Figure 11. van Dokkum et al. (2015) quoted a threshold in velocity dispersion of $225\,\mathrm{km\,s}^{-1}$, based on an analysis of compact star-forming galaxies at $1.5 < z < 3.0$ with a median size is $r_e = 1.8$ kpc. When correcting to $r = 1$ kpc following Cappellari et al. (2006), this quenching threshold increases to $234\,\mathrm{km\,s}^{-1}$. This is equivalent to a central circular velocity of $\sim 331\,\mathrm{km\,s}^{-1}$, assuming $v_{circ} = \sqrt{2}\,\sigma$.

Finally, we show the central densities of quiescent galaxies in grayscale in Figure 11, with the running median shown in red. Although these high central densities are probably reliable because the measured r_e and n were only considered in the case of a sufficiently high S/N, we cannot rule out that they are biased low at the highest redshifts as a consequence of resolution limitations. However, Figure 12 shows the results of the error analysis on the data presented in Figure 9, showing that the error of the mean ρ_1 is smallest for galaxies with high n. The error analysis accounts for the covariance of the parameters, as described in Section 2.4. Even though the bin of the smallest galaxies has the largest uncertainty in ρ_1, the errors are not large enough to significantly affect the trends we see in Figure 11. The median central density of quiescent galaxies at a given epoch is similar to our quenching threshold based on an evolving threshold in sSFR. If we were instead to see that these quiescent galaxies had even higher central densities, this would suggest that the threshold we find is too low, as otherwise the star-forming galaxies would need to be able to continue to form more stars and further increase their central mass concentrations. The results of Bezanson et al. (2009) show that the central densities of high-redshift galaxies are slightly higher than low-redshift ellipticals. As we observe galaxies to puff up over time via minor mergers and accretion (e.g., Newman et al. 2012), this suggests that although quiescent galaxies grow in size with time, their central densities will probably not continue to increase once quenched, and may decrease slightly. As these quiescent galaxies must have reached this threshold at earlier times, their distribution of central densities with redshift suggests that the evolution of the quenching threshold slows down above $z \sim 2$. It is unclear whether this evolution in the quenching threshold is physical or simply an artifact of other processes that trigger the shutdown of star formation. Although it is difficult to interpret the

Table 2
Broken Power-law Fits: log(sSFR)–log(ρ_1)

	All Galaxies				UVJ Star-forming			
Redshift Range	a_{low}	a_{high}	b	c	a_{low}	a_{high}	b	c
$0.5 < z < 1.0$	-0.16 ± 0.03	-1.16 ± 0.04	8.43 ± 0.04	-9.16 ± 0.03	-0.09 ± 0.03	-0.80 ± 0.05	8.42 ± 0.05	-9.08 ± 0.02
$1.0 < z < 1.5$	-0.08 ± 0.03	-1.21 ± 0.06	8.75 ± 0.04	-8.93 ± 0.02	-0.00 ± 0.04	-0.46 ± 0.05	8.43 ± 0.08	-8.84 ± 0.02
$1.5 < z < 2.5$	-0.10 ± 0.02	-1.08 ± 0.07	8.92 ± 0.05	-8.75 ± 0.02	-0.03 ± 0.03	-0.45 ± 0.06	8.77 ± 0.09	-8.68 ± 0.02

Note. Broken power-law coefficients parameterizing the evolution of the log(sSFR)–log(ρ_1) relation from the median stacking analysis (Equation (3)). a_{low} signifies the best-fit slope for galaxies below the characteristic stellar mass density Σ_1, and a_{high} is the slope above this limit.

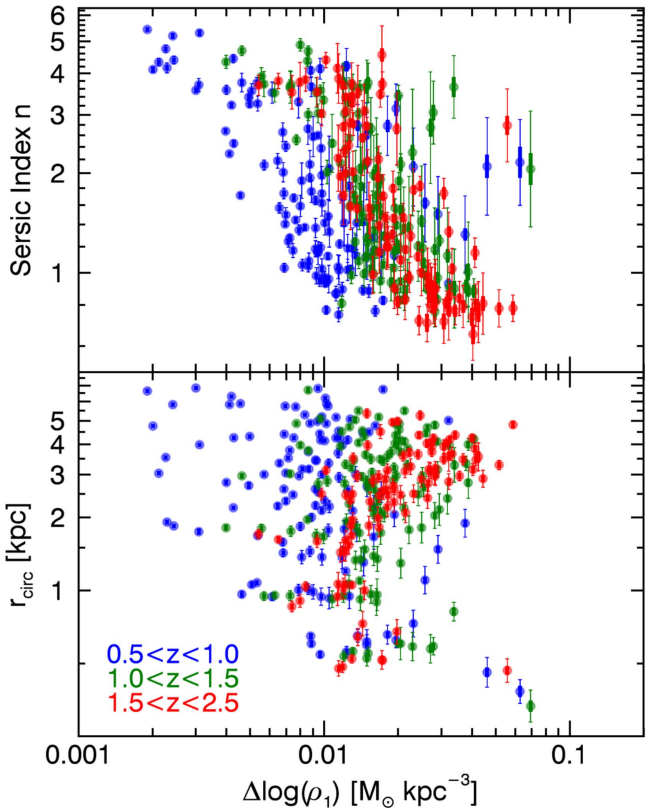

Figure 12. The error analysis on the data presented in Figure 9 reveals that galaxies with the lowest n generally have the largest uncertainty in ρ_1. The thin error bars represent the errors of all galaxies in that bin added in quadrature, while the thick error bars represent the error in the mean. The trend between the uncertainty in ρ_1 and circularized r_e is less clear, except for the most extreme small galaxy bins with the largest errors in ρ_1. The error in ρ_1 is generally larger at $z > 1$.

meaning behind this evolving quenching threshold, the observed central densities of quiescent galaxies with redshift indicate that quiescence should not be defined as a non-evolving limit of log(sSFR) $= -10$. Spatially resolved absorption line studies of the steller populations with extremely deep data sets such as the upcoming LEGA-C survey at $z \sim 1$ (van der Wel et al. 2016) will potentially constrain the timescale for quenching and also better quantify the physical parameters predicting quiescence.

5. Discussion

Theoretical predictions for the interplay between galaxy structures and their star formation histories are far from reaching a consensus. In this section we summarize some of the key predictions and compare them to the empirical results from this paper. We place emphasis on the quenching process, which must both truncate star formation and structurally transform galaxies as they migrate from a star-forming population to a quiescent one. Although the current analysis does not suggest an overall residual correlation between SFR and galaxy effective radius, we have identified a population of compact intermediate-mass star-forming galaxies with depressed SFRs. Focusing specifically on this population of compact, likely quenching galaxies, we discuss whether theoretical studies predict their existence.

There are two main channels in cosmological simulations to form massive compact galaxy populations: (1) the galaxies have very early formation times when the universe was far denser (Khochfar & Silk 2006; Wellons et al. 2015), or (2) they are the result of a central starburst driven by violent disk instabilities (Ceverino et al. 2015; Zolotov et al. 2015) or gas-rich mergers (Wellons et al. 2015). However, it may also be that galaxies do not undergo such "compaction" events, and that compact galaxies simply evolved from slightly smaller galaxies with lower mass (van Dokkum et al. 2015).

In cosmological simulations by Tacchella et al. (2016), where a central starburst drives structural evolution, the gas and young stars in galaxies with high sSFRs (above the average star formation sequence) are predicted to be compact with short gas-depletion timescales. Tacchella et al. (2016) did not, however, find any gradients in the stellar mass distribution that traces the older stellar distribution. When we consider only the galaxies with compact rest-frame 5000 Å sizes in this study, we similarly do not see evidence that they have sSFRs that are higher than average. If anything, we see the opposite trend, at least among the most compact intermediate stellar mass galaxies ($\log(M_\star/M_\odot) \sim 10.0$–$10.6$). Such fading galaxies appear to be absent in the Tacchella simulations, based on their mass-weighted sizes. Results from the EAGLE simulation (at $z = 0$), on the other hand, predict a stronger dependence of galaxy size on sSFR than our higher redshift observations (Figure 2 in Furlong et al. 2017), with $\Delta\log(\mathrm{sSFR})/\Delta\log(r_e)$ at fixed stellar mass ranging between $\sim$0.6 and 1.4 compared to typical values of $\sim$0.1–0.5 in the observations. Using semi-analytic models, Brennan et al. (2017) showed a weak(er) trend among the most compact galaxies at $z = 0$–2.5 that falls between these two extremes, although the comparison cannot be made directly as the stellar mass dependence has not been factored out. In summary, theoretical results predict a range from no residual dependence of galaxy size on SFR to moderately strong trends.

One key trend that the EAGLE simulations do not reproduce among the star-forming population is the lack of variation in

sSFR at lower stellar masses. While this model shows variations on the order of 0.3–0.5 dex, the variation in sSFR within the five extragalactic fields included in the 3D-*HST* data set is <0.2 dex. Unfortunately, Furlong et al. (2017) did not present their higher redshift results, so that a more direct comparison at the equivalent epochs is not possible. Similarly, this information cannot be reconstructed from the results of Tacchella et al. (2016) and Brennan et al. (2017). Future comparisons like this between the observations and theoretical models will prove illuminating.

Returning to the issue of gas depletion in relation to compaction, a recent study by Spilker et al. (2016) found extremely low (CO) gas fractions in a pilot sample of compact star-forming galaxies, suggesting short gas-depletion timescales. As these compact star-forming galaxies exist in very small numbers, they would need to quench rapidly (<0.5 Gyr timescales) in order to produce the required number of compact quiescent galaxies (van Dokkum et al. 2015). The early results on the gas depletion timescales indeed suggest timescales on the order of 100 Myr or shorter (Barro et al. 2016; Spilker et al. 2016). Saintonge et al. (2012) also showed that galaxies undergoing mergers or showing signs of morphological disruptions have the shortest molecular gas depletion times. These results indicate that the timescale for galaxies to pass through this compact high sSFR phase is short, and therefore observational evidence is lacking when considering the average trends presented here.

Next, we focus again on the full galaxy population. The remarkably small scatter and the evolution of the average relation between sSFR and central density are both interesting in the context of recent arguments in the literature regarding the the nature of the most recently quenched galaxies and their role in the evolution of the size–mass relation of quiescent galaxies. Although it has been shown that quiescent galaxies will experience growth through minor mergers and accretion (Bezanson et al. 2009; Newman et al. 2012), the simplest explanation of their size growth is the continuous addition of (larger) recently quenched galaxies (van der Wel et al. 2009). Galaxies that quench at later times are expected to have larger sizes because the universe was less dense and therefore gas rich, dissipative processes were less efficient (Khochfar & Silk 2006). Observations at $z < 1$ found that the most recently quenched galaxies are the largest (Carollo et al. 2013). There are widely varying size measurements at $z \sim 1.5$ (Belli et al. 2015), with recently quenched galaxies exhibiting a range of sizes, and results at $z > 1.5$ find that the most recently quenched galaxies are similar, if not more compact, than older quiescent galaxies at the same epoch (Whitaker et al. 2012b; Yano et al. 2016). Furlong et al. (2017) furthermore predicted a trend (at $z = 0$) for higher sSFR (suggesting more recent assembly) for larger quiescent galaxies at fixed stellar mass. We do not see any strong trends among our quiescent observations at $z > 0.5$. As the 24 μm derived SFRs are very likely upper limits for quiescent galaxies, it is possible that we are diluting a stronger intrinsic trend within the observations. It may be that recently quenched galaxies are more compact at high redshift and are larger at later times. At $z > 1$, we show here that the central density threshold for quenching is higher than the already quenched population in Figure 11 (shown as grayscale, with the running median in red). We therefore see evidence that higher redshift quiescent galaxies are predicted to have significantly higher central densities to quench, which may therefore alleviate some of the contradiction in the observations between lower and higher redshift analyses.

When considering where massive galaxies populate the log (sSFR)–log(ρ_1) plane (e.g., Figure 10), we see that they tend to have the densest central concentrations of stellar mass. It is important to note, however, that the trend itself between central density and sSFR does not vary strongly with stellar mass at a given epoch. In other words, while different stellar mass regimes tend to populate the upper and lower end of this relation, the entire relation itself evolves with redshift. Although there is no straightforward way to plot the results of Barro et al. (2015) in the $\Delta \log(\mathrm{SFR})$–$\Delta \log(\Sigma_1)$ plane in our Figure 11, they are in good qualitative agreement given the definition of $\Delta \log(\Sigma_1)$. The stellar mass dependence of this quenching threshold in central density observed by Fang et al. (2013) at $z = 0$ may also be explained in part by more massive galaxies having formed earlier in the universe (Kauffmann et al. 2003a). A thorough discussion of this downsizing in quenching is provided in Dekel & Burkert (2014). As more massive dark matter halos will tend to cross a threshold halo mass for viral shock heating earlier in the universe, halo quenching will occur preferentially in more massive galaxies (e.g., Neistein et al. 2006; Bouché et al. 2010). Similarly, violent disk instabilities will also have a natural downsizing, which Dekel & Burkert (2014) argued is the result of higher gas fractions in lower mass galaxies. Whether galaxies quench fast through, e.g., violent disk instabilities, or slow through halo quenching, more massive galaxies will tend to cross this quenching threshold earlier in time.

The predicted redshift evolution of the quenching threshold for central galaxies from Voit et al. (2015) is shown as a thin black line in Figure 11. Their paper presents an argument for self-regulated feedback that links a galaxy star formation history directly with the circular velocity of its potential well. Voit et al. (2015) hypothesized that feedback leads to quenching when the halo mass reaches a critical value that allows supernovae and/or AGN to push the rest of the circumgalactic gas away. This critical circular velocity is set to 300 km s^{-1} at $z = 2$ here, resulting in a quenching threshold that tracks the upper envelope of the central density observed for the quiescent population.

In Figure 11 we show that the quenching threshold differs from the characteristic turnover value. This difference may either imply that galaxies continue to grow their centers after star formation begins to actively diminish. Alternatively, there might be significant scatter in this quenching threshold, where galaxies with central densities in between the characteristic turnover and the quenching threshold have an intermediate probability of being quenched.

Although we observe that a high central density appears to predict quiescence on average, we caution that this does not necessarily imply causation. Lilly & Carollo (2016) proposed instead that galaxies quench their star formation according to empirical probabilistic laws that depend solely on the total mass of the galaxy, not on the surface mass density or size. With their simple model they were able to broadly reproduce all of the trends between galaxy structure and sSFR that we observe here, including the evolving quenching threshold. Lilly

& Carollo (2016) argued that because galaxies form their stars inside-out and passive galaxies will form them at earlier epochs (higher redshifts), passive galaxies will always have smaller sizes than their star-forming counterparts of the same stellar mass at any given redshift. Determining the cause of quenching is beyond the scope of this paper, but we note that even without causation, we show that the high central density holds a unique predictive power in identifying the population of galaxies that, on average, will be quiescent.

6. Summary

The aim of this paper was to connect rest-frame optical measurements of the size–mass and density–mass relations with trustworthy measurements of the total specific SFRs from a purely empirical standpoint. We thereby connected galaxy structure and star formation to better understand the observed bimodal distribution of galaxies across cosmic time and the quenching of star formation. This current study extends the original work by Franx et al. (2008) on a smaller field that included 1155 galaxies at $0.2 < z < 3.5$ to now consider a mass-complete sample of 27,893 galaxies at $0.5 < z < 2.5$. The sample was selected in five extragalactic fields from the 3D-*HST* photometric catalogs presented in Skelton et al. (2014), combining high spatial resolution *HST* NIR imaging from the CANDELS treasury program with total UV+IR SFRs derived from a median stacking analysis of *Spitzer*/MIPS 24 μm imaging.

The main results presented in this paper are summarized as follows.

1. We find that 50% of new stars being formed among the overall population occurs in galaxies within ± 0.13 dex of the average size–mass relation. Extremely compact or extended galaxies do not significantly contribute to the total stellar mass budget.
2. We show a flattening in the size–mass relation of quiescent galaxies at stellar masses below 10^{10} $M_{\odot}$ at $0.5 < z < 1.0$. These quiescent galaxies with lower mass exhibit slightly higher sSFRs than more massive galaxies at the same epoch, suggesting more recent assembly. However, the sSFRs of quiescent galaxies at fixed stellar mass do not show significant variations.
3. After removing the well-known correlations between stellar mass and SFR and galaxy size, we showed that the SFR of star-forming galaxies is weakly dependent on galaxy size. The residual offset in size for star-forming galaxies in the lowest quartile when rank-ordered by sSFR is 0.27 ± 0.06 dex smaller than the highest sSFR quartile. Similarly, when we instead rank-order them by the residual size offsets, the smallest galaxies have lower sSFRs by 0.11 ± 0.02 dex than that of the largest galaxy quartile. Similar trends are found among massive galaxies in simulations (e.g., Furlong et al. 2017), although greatly amplified compared to the observations.
4. We find that the independence of SFR on galaxy size is not sensitive to the timescale on which the SFR is probed, with dust-corrected Hα sSFRs yielding similar trends.
5. We confirm earlier studies (e.g., Franx et al. 2008), showing that the central stellar density is a key parameter connecting galaxy morphology and star formation histories: stacks of galaxies with high central densities are red and have increasingly lower sSFRs, whereas galaxies stacked with low central densities are blue and have a roughly constant (higher) sSFRs at a given redshift interval.
6. We used a broken power law to parameterize the correlation between log(sSFR) and central density, log (ρ_1), which showed remarkably little scatter between the average measurements.
7. We found a strong evolution in the central density threshold for quenching, as defined by both a constant and evolving threshold in sSFR that decreases by >0.5 dex from $z \sim 2$ to $z \sim 0.7$. Similarly, while the threshold in central circular velocity where most galaxies are considered quenched is $>300\,\mathrm{km\,s^{-1}}$ at $z \sim 2$, this decreases to $\sim 150\,\mathrm{km\,s^{-1}}$ by $z \sim 0.7$.

We showed that neither a high n nor a compact galaxy size will uniquely predict quiescence, whereas a threshold in central density (or velocity) may be a more reliable and unique observable signature when considering the overall galaxy population. However, we emphasize that correlations between structure and star formation do not prove a causal effect. For example, it remains to be seen whether small-scale structure (at the scale of the stars) or large-scale parameters (the scale of the dark matter halo) dominate the physical processes that quench galaxies. While we have presented the average global trends of the sSFR with structural parameters (r_e, n, Σ_e, ρ_1, and $v_{\mathrm{circ},1}$) in a mass-complete sample of galaxies using high-resolution *HST*/WFC3 imaging and deep *Spitzer*/MIPS 24 μm imaging, future studies with the *James Webb Space Telescope* mid-IR spectroscopic and photometric capabilities will yield reliable measurements of SFR for individual galaxies across the star formation sequence. Such studies will allow us to resolve the detailed trends within the star-forming population as a function of structure.

We thank the anonymous referee for useful comments and a careful reading of the paper. The authors wish to acknowledge Sandy Faber and Mark Voit for helpful discussions. K.E.W. gratefully acknowledges support by NASA through Hubble Fellowship grant #HST-HF2-51368 awarded by the Space Telescope Science Institute, which is operated by the Association of Universities for Research in Astronomy, Inc., for NASA, under contract NAS 5-26555. The authors are grateful to the many colleagues who have provided public data and catalogs in the five deep 3D-*HST* fields; high-redshift galaxy science has thrived owing to this gracious mindset and the TACs and the Observatory Directors who have encouraged this. This work is based on observations taken by the 3D-*HST* Treasury Program (GO 12177 and 12328) with the NASA/ESA *HST*, which is operated by the Associations of Universities for Resarch in Astronomy, Inc., under NASA contract NAS5-26555.

Appendix

In order to remove the well-known correlations between SFR and galaxy size with stellar mass and redshift, we fit the best-fit coefficients describing the log(SFR)–log($M_\star$) relations in Whitaker et al. (2014) and the log(r_e)–log($M_\star$) relation in

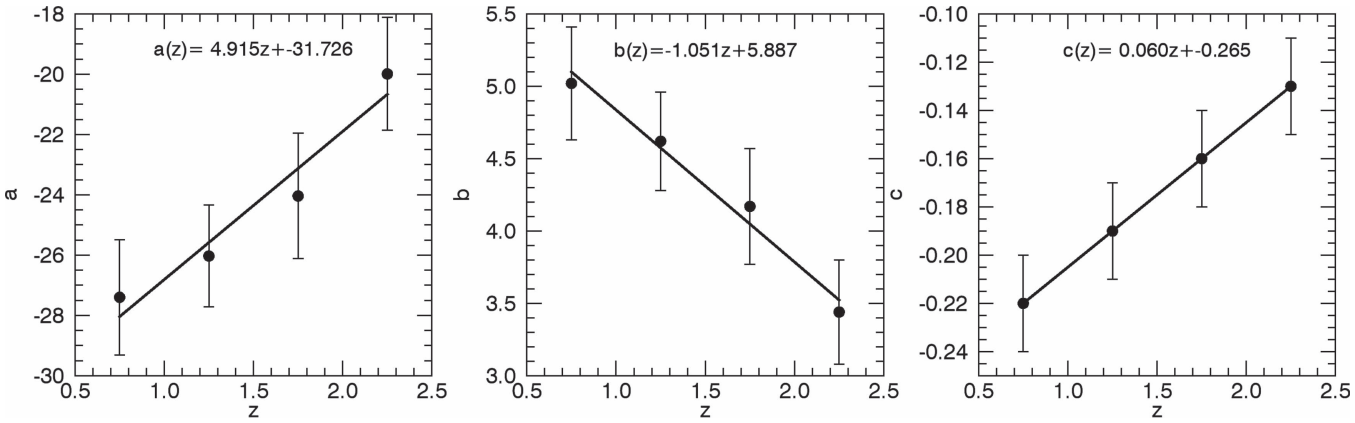

Figure 13. Redshift evolution of the best-fit polynomial coefficients to the average observed logarithmic relation between star formation rate and stellar mass from Whitaker et al. (2014). The linear coefficients defining the black solid lines in each panel are listed at the top of each panel.

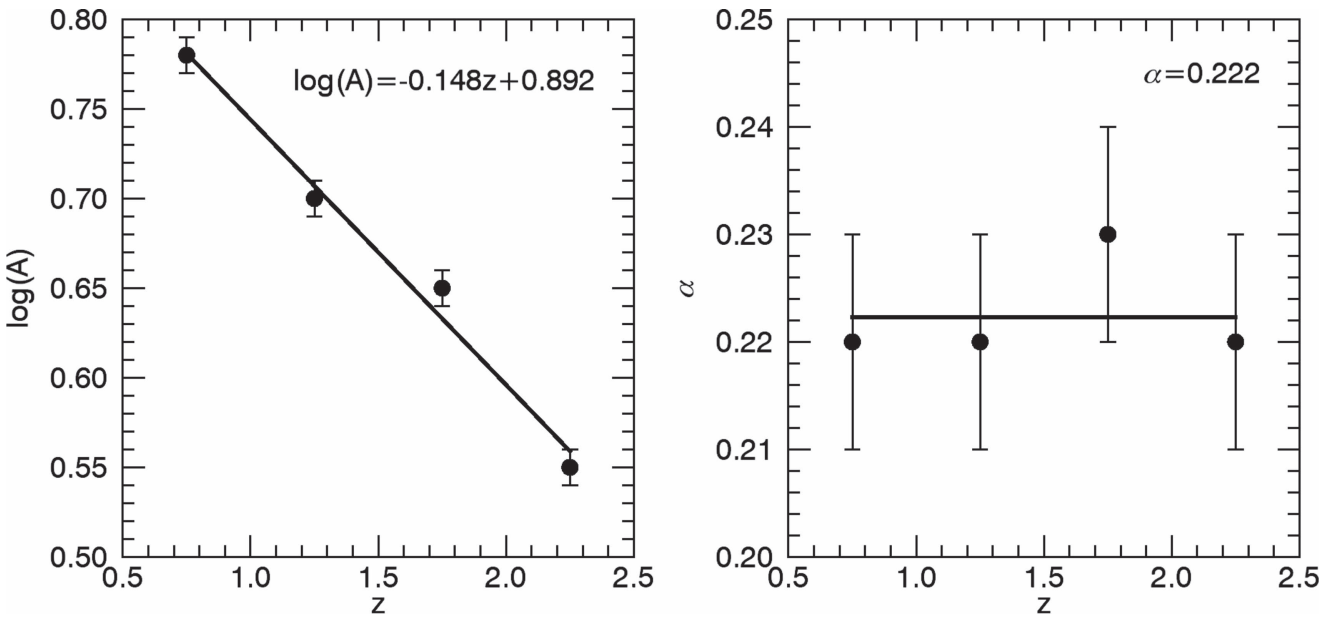

Figure 14. Redshift evolution of the best-fit coefficients to the average observed logarithmic relation between galaxy size and stellar mass from van der Wel et al. (2014). The linear coefficients defining the black solid lines are listed at the top of each panel.

van der Wel et al. (2014). The method and data are identical for the present study and these earlier works.

The measured log(SFR)–log($M_\star$) relation is defined in Equation (2) of Whitaker et al. (2014). In Figure 13 we fit the redshift evolution of the observed relations with simple least-squares linear fits for the three polynomial coefficients, weighted by their respective uncertainties. We therefore parameterize the stellar mass and redshift dependence of the star formation sequence as follows,

$$\log \mathrm{SFR}(z, M_\star) = [a_1 z + a_2] + [b_1 z + b_2]\log\left(\frac{M_\star}{M_\odot}\right) + [c_1 z + c_2]\log\left(\frac{M_\star}{M_\odot}\right)^2, \quad (4)$$

where the best-fit parameters describing the redshift evolution of the polynomial coefficients are presented at the top of each panel in Figure 13.

In order to remove the average redshift and stellar mass dependence on galaxy size, we also subtract the following stellar mass and redshift dependent log(r_e)–log($M_\star$) relation from Figure 14:

$$\log r_e(z, M_\star) = [\log(A_1) z + \log(A_2)] + [\alpha_1 z + \alpha_2] \times [\log(M_\star) - \log(5 \times 10^{10}\, M_\odot)], \quad (5)$$

with the best-fit redshift evolution of the normalization to the size–mass relation presented at the top of the left panel in Figure 14. The slope of the size–mass relation for star-forming galaxies only is assumed to be roughly constant, with $\alpha = 0.22$. Given the average redshift and stellar mass of each bin across the size–mass plane, we use the two equations above to subtract the average correlations.

We present the same data in Figure 15 as in Figure 1, the rest-frame 5000 Å size of galaxies as a function of their stellar mass in three redshift intervals, but instead color-coded by the logarithmic deviation from the average log(SFR)–log($M_\star$)

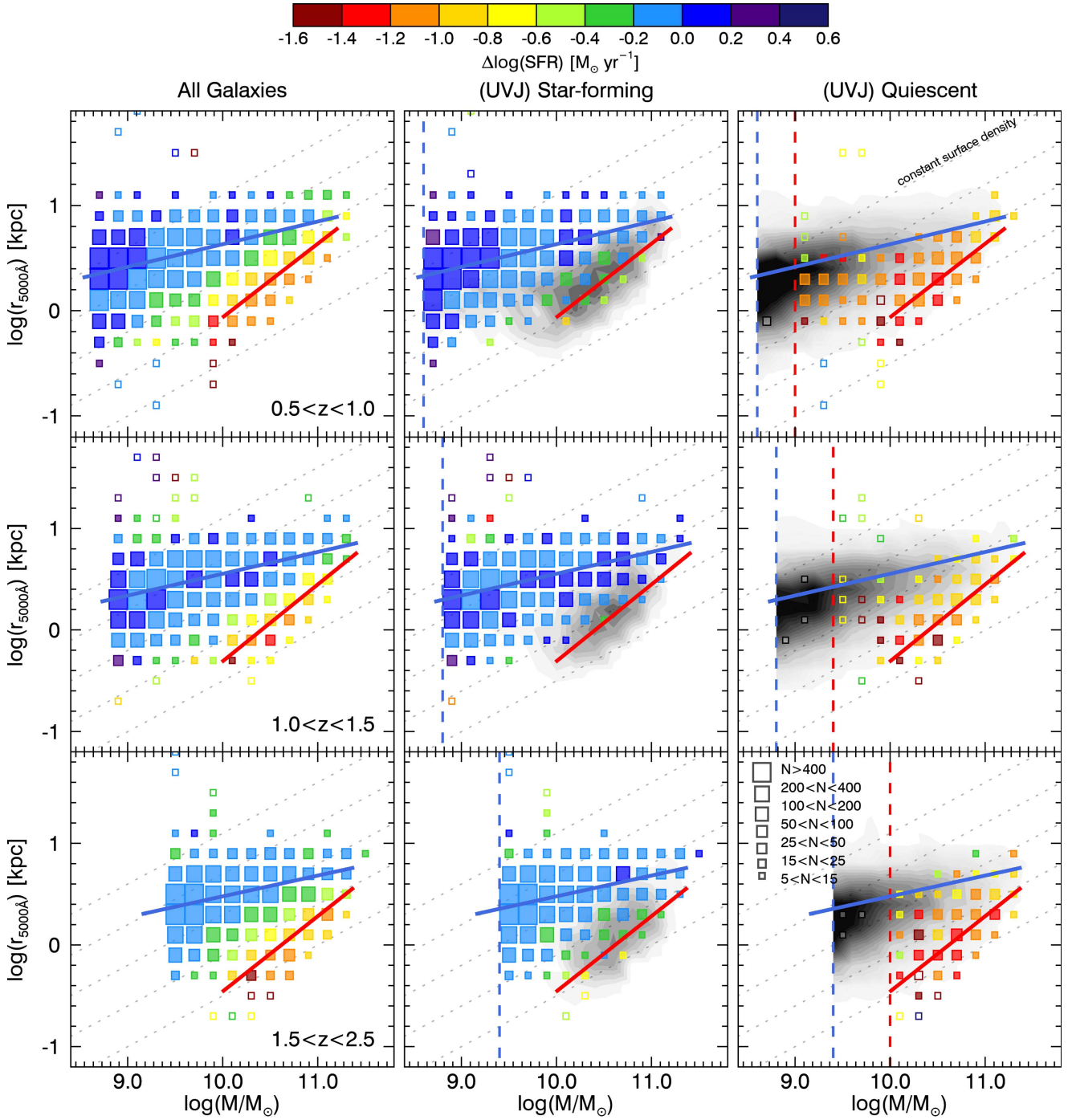

Figure 15. Rest-frame 5000 Å size of galaxies as a function of stellar mass, color-coded by the logarithmic deviation from the average log(SFR)–log($M_\star$) relation in 0.2 dex bins. The size of the symbol depends on the number of galaxies that enter each bin. The vertical dashed lines correspond to the stellar mass limits down to which the structural parameters can be trusted for star-forming (blue) and quiescent (red) populations.

relation as defined in Equation (4). While we no longer see the turnover toward lower sSFRs in the log(SFR)–log($M_\star$) relation at the massive end by definition, we instead highlight this lower envelope of compact galaxies with decreased star formation efficiency. These galaxies are also evident in Figure 3, which also takes the size–mass relation as defined in Equation (5) into account. Figure 15 shows that typical larger star-forming galaxies have SFRs consistent within 1σ with the log(SFR)–log($M_\star$) relation at each epoch. These results support the main conclusion reached more quantitatively from Figure 2.

References

Abramson, L. E., & Morishita, T. 2016, ApJL, submitted (arXiv:1608.07577)
Barro, G., Faber, S. M., Koo, D. C., et al. 2015, ApJ, submitted (arXiv:1509.00469)
Barro, G., Faber, S. M., Pérez-González, P. G., et al. 2013, ApJ, 765, 104
Barro, G., Kriek, M., Pérez-González, P. G., et al. 2016, ApJL, 827, L32
Bell, E. F., van der Wel, A., Papovich, C., et al. 2012, ApJ, 753, 167
Belli, S., Newman, A. B., & Ellis, R. S. 2015, ApJ, 799, 206
Bezanson, R., van Dokkum, P. G., Tal, T., et al. 2009, ApJ, 697, 1290
Bluck, A. F. L., Mendel, J. T., Ellison, S. L., et al. 2014, MNRAS, 441, 599
Boada, S., Tilvi, V., Papovich, C., et al. 2015, ApJ, 803, 104

Bouché, N., Dekel, A., Genzel, R., et al. 2010, ApJ, 718, 1001
Brammer, G. B., van Dokkum, P. G., Franx, M., et al. 2012, ApJS, 200, 13
Brennan, R., Pandya, V., Somerville, R. S., et al. 2015, MNRAS, 451, 2933
Brennan, R., Pandya, V., Somerville, R. S., et al. 2017, MNRAS, 465, 619
Brinchmann, J., Charlot, S., White, S. D. M., et al. 2004, MNRAS, 351, 1151
Bruce, V. A., Dunlop, J. S., Cirasuolo, M., et al. 2012, MNRAS, 427, 1666
Bruce, V. A., Dunlop, J. S., McLure, R. J., et al. 2014, MNRAS, 444, 1660
Cappellari, M., Bacon, R., Bureau, M., et al. 2006, MNRAS, 366, 1126
Cappellari, M., McDermid, R. M., Alatalo, K., et al. 2013, MNRAS, 432, 1862
Carollo, C. M., Bschorr, T. J., Renzini, A., et al. 2013, ApJ, 773, 112
Ceverino, D., Dekel, A., Tweed, D., et al. 2015, MNRAS, 447, 3291
Chabrier, G. 2003, PASP, 115, 763
Cheung, E., Faber, S. M., Koo, D. C., et al. 2012, ApJ, 760, 131
Cimatti, A., Cassata, P., Pozzetti, L., et al. 2008, A&A, 482, 21
Ciotti, L. 1991, A&A, 249, 99
Ciotti, L., & Bertin, G. 1999, A&A, 352, 447
Dekel, A., & Burkert, A. 2014, MNRAS, 438, 1870
Dickinson, M. & FIDEL Team 2007, BAAS, 39, 822
Dickinson, M., Papovich, C., Ferguson, H. C., et al. 2003, ApJ, 587, 25
Donley, J. L., Koekemoer, A. M., Brusa, M., et al. 2012, ApJ, 748, 142
Elbaz, D., Daddi, E., Le Borgne, D., et al. 2007, A&A, 468, 33
Fang, J. J., Faber, S. M., Koo, D. C., et al. 2013, ApJ, 776, 63
Franx, M., van Dokkum, P. G., Schreiber, N. M. F., et al. 2008, ApJ, 688, 770
Fumagalli, M., Labbé, I., Patel, S. G., et al. 2014, ApJ, 796, 35
Furlong, M., Bower, R. G., Crain, R. A., et al. 2017, MNRAS, 465, 722
Genzel, R., Förster Schreiber, N. M., Lang, P., et al. 2014, ApJ, 785, 75
Genzel, R., Tacconi, L. J., Lutz, D., et al. 2015, ApJ, 800, 20
Grogin, N. A., Kocevski, D. D., Faber, S. M., et al. 2011, ApJS, 197, 35
Guo, Y., Giavalisco, M., Cassata, P., et al. 2011, ApJ, 735, 18
Guo, Y., Giavalisco, M., Ferguson, H. C., et al. 2012, ApJ, 757, 120
Guo, Y., McIntosh, D. H., Mo, H. J., et al. 2009, MNRAS, 398, 1129
Häussler, B., McIntosh, D. H., Barden, M., et al. 2007, ApJS, 172, 615
Hayward, C. C., Lanz, L., Ashby, M. L. N., et al. 2014, MNRAS, 445, 1598
Huertas-Company, M., Shankar, F., Mei, S., et al. 2013, ApJ, 779, 29
Kauffmann, G., Heckman, T. M., White, S. D. M., et al. 2003a, MNRAS, 341, 33
Kauffmann, G., Heckman, T. M., White, S. D. M., et al. 2003b, MNRAS, 341, 54
Khochfar, S., & Silk, J. 2006, ApJL, 648, L21
Koekemoer, A. M., Faber, S. M., Ferguson, H. C., et al. 2011, ApJS, 197, 36
Kriek, M., van Dokkum, P. G., Franx, M., et al. 2009, ApJL, 705, L71
Lang, P., Wuyts, S., Somerville, R. S., et al. 2014, ApJ, 788, 11
Lee, N., Sanders, D. B., Casey, C. M., et al. 2015, ApJ, 801, 80
Lilly, S. J., & Carollo, C. M. 2016, ApJ, 833, 14
Maier, C., Lilly, S. J., Zamorani, G., et al. 2009, ApJ, 694, 1099
Martig, M., Bournaud, F., Teyssier, R., et al. 2009, ApJ, 707, 250
Martig, M., Crocker, A. F., Bournaud, F., et al. 2013, MNRAS, 432, 1914
McDermid, R. M., Alatalo, K., Blitz, L., et al. 2015, MNRAS, 448, 3484
Momcheva, I. G., Brammer, G. B., van Dokkum, P. G., et al. 2016, ApJS, 225, 27
Morishita, T., Ichikawa, T., Noguchi, M., et al. 2015, ApJ, 805, 34
Muzzin, A., Marchesini, D., Stefanon, M., et al. 2013, ApJS, 206, 8
Neistein, E., van den Bosch, F. C., & Dekel, A. 2006, MNRAS, 372, 933
Nelson, E. J., van Dokkum, P. G., Förster Schreiber, N. M., et al. 2016a, ApJ, 828, 27
Nelson, E. J., van Dokkum, P. G., Momcheva, I. G., et al. 2016b, ApJL, 817, L9
Newman, A. B., Ellis, R. S., Bundy, K., et al. 2012, ApJ, 746, 162
Norris, M. A., Kannappan, S. J., Forbes, D. A., et al. 2014, MNRAS, 443, 1151
Omand, C. M. B., Balogh, M. L., & Poggianti, B. M. 2014, MNRAS, 440, 843
Rodighiero, G., Daddi, E., Baronchelli, I., et al. 2011, ApJL, 739, L40
Saintonge, A., Tacconi, L. J., Fabello, S., et al. 2012, ApJ, 758, 73
Sanders, D. B., Salvato, M., Aussel, H., et al. 2007, ApJS, 172, 86
Saracco, P., Gargiulo, A., & Longhetti, M. 2012, MNRAS, 422, 3107
Schreiber, C., Elbaz, D., Pannella, M., et al. 2016, A&A, 589, 35
Schreiber, C., Pannella, M., Elbaz, D., et al. 2015, A&A, 575, A74
Shankar, F., Mei, S., Huertas-Company, M., et al. 2014, MNRAS, 439, 3189
Shen, S., Mo, H. J., White, S. D. M., et al. 2003, MNRAS, 343, 978
Simpson, J. M., Smail, I., Swinbank, A. M., et al. 2015, ApJ, 799, 81
Skelton, R. E., Whitaker, K. E., Momcheva, I. G., et al. 2014, ApJS, 214, 24
Speagle, J. S., Steinhardt, C. L., Capak, P. L., et al. 2014, ApJS, 214, 15
Spilker, J. S., Bezanson, R., Marrone, D. P., et al. 2016, ApJ, 832, 19
Szomoru, D., Franx, M., van Dokkum, P. G., et al. 2010, ApJL, 714, L244
Szomoru, D., Franx, M., van Dokkum, P. G., et al. 2013, ApJ, 763, 73
Tacchella, S., Carollo, C. M., Renzini, A., et al. 2015a, Sci, 348, 314
Tacchella, S., Dekel, A., Carollo, C. M., et al. 2016, MNRAS, 457, 2790
Tacchella, S., Lang, P., Carollo, C. M., et al. 2015b, ApJ, 802, 101
Tacconi, L. J., Genzel, R., Neri, R., et al. 2010, Natur, 463, 781
Tacconi, L. J., Neri, R., Genzel, R., et al. 2013, ApJ, 768, 74
Tadaki, K.-i., Kohno, K., Kodama, T., et al. 2015, ApJL, 811, L3
Tal, T., Dekel, A., Oesch, P., et al. 2014, ApJ, 789, 164
Taylor, E. N., Franx, M., Glazebrook, K., et al. 2010, ApJ, 720, 723
Teimoorinia, H., Bluck, A. F. L., & Ellison, S. L. 2016, MNRAS, 457 2086
Thomas, D., Maraston, C., Bender, R., et al. 2005, ApJ, 621, 673
Tomczak, A. R., Quadri, R. F., Tran, K.-V. H., et al. 2016, ApJ, 817, 118
Trujillo, I., Conselice, C. J., Bundy, K., et al. 2007, MNRAS, 382, 109
Utomo, D., Kriek, M., Labbé, I., et al. 2014, ApJL, 783, L30
van der Wel, A., Bell, E. F., Häussler, B., et al. 2012, ApJS, 203, 24
van der Wel, A., Bell, E. F., van den Bosch, F. C., et al. 2009, ApJ, 698, 1232
van der Wel, A., Franx, M., van Dokkum, P. G., et al. 2014, ApJ, 788, 28
van der Wel, A., Holden, B. P., Zirm, A. W., et al. 2008, ApJ, 688, 48
van der Wel, A., Noeske, K., Bezanson, R., et al. 2016, ApJS, 223, 29
van Dokkum, P. G., Bezanson, R., van der Wel, A., et al. 2014, ApJ, 791, 45
van Dokkum, P. G., Nelson, E. J., Franx, M., et al. 2015, ApJ, 813, 23
van Dokkum, P. G., Whitaker, K. E., Brammer, G., et al. 2010, ApJ, 709, 1018
Voit, G. M., Bryan, G. L., O'Shea, B. W., et al. 2015, ApJL, 808, L30
Wake, D. A., van Dokkum, P. G., & Franx, M. 2012, ApJL, 751, L44
Wellons, S., Torrey, P., Ma, C.-P., et al. 2015, MNRAS, 449, 361
Whitaker, K. E., Franx, M., Bezanson, R., et al. 2015, ApJL, 811, L12
Whitaker, K. E., Franx, M., Leja, J., et al. 2014, ApJ, 795, 104
Whitaker, K. E., Kriek, M., van Dokkum, P. G., et al. 2012a, ApJ, 745, 179
Whitaker, K. E., van Dokkum, P. G., Brammer, G., et al. 2012b, ApJL, 754, L29
Williams, R. J., Quadri, R. F., Franx, M., et al. 2010, ApJ, 713, 738
Woo, J., Dekel, A., Faber, S. M., et al. 2015, MNRAS, 448, 237
Wuyts, S., Förster Schreiber, N. M., Genzel, R., et al. 2012, ApJ, 753, 114
Wuyts, S., Förster Schreiber, N. M., Lutz, D., et al. 2011a, ApJ, 738, 106
Wuyts, S., Förster Schreiber, N. M., van der Wel, A., et al. 2011b, ApJ, 742, 96
Wuyts, S., Labbé, I., Schreiber, N. M. F., et al. 2008, ApJ, 682, 985
Yano, M., Kriek, M., van der Wel, A., et al. 2016, ApJL, 817, L21
Zolotov, A., Dekel, A., Mandelker, N., et al. 2015, MNRAS, 450, 2327